# Stator Design of an AFPMSM for Aerospace Applications

# On the stator design of an axial flux permanent magnet synchronous traction machine for aerospace applications

By

Cyrille Goldstein, B.Eng.

*A Thesis*

*Submitted to the Department of Electrical and Computer Engineering*

*and the School of Graduate Studies of McMaster University*

*in Partial Fulfillment of the Requirements for the Degree of*

*Master of Applied Science*

McMaster University
Master of Applied Science (2021)
Hamilton, Ontario, Canada (Electrical and Computer Engineering)

| | |
|---|---|
| Title: | On the Stator Design of an Axial Flux Permanent Magnet Synchronous Traction Machine for Aerospace Applications |
| Author: | Cyrille Goldstein<br>B.Eng. (McGill University) |
| Supervisor: | Dr. Ali Emadi<br>Ph.D. (Texas A&M University) |
| Number of Pages: | xvii, 111 |

# Abstract

Aviation is one of the fastest growing methods of transportation, with passenger volumes expected to triple in the next twenty-five years. It is also contributing an ever increasing share of global emissions. One of the highly effective ways to reduce emissions in aerospace is through electrification. This is already underway with the development and adoption of More Electric Aircraft. A next step is the development of hybrid propulsion, or all electric aircraft, with electric propulsion systems. In order to achieve this goal, the power density of the electric drive is of critical importance. Axial flux permanent magnet synchronous machines have been identified as one the highest power density machine types suitable for these electric drives.

In this thesis, an axial flux permanent magnet machine is developed for an electric aircraft propulsion system. A review of electric machines in aerospace applications is conducted, followed by an overview of the design and simulation of axial flux machines, and a presentation of the machine under study. The primary objective of this thesis is to improve the stator design of the axial flux machine by reducing loss, weight, and volume. Magnetic materials are studied, and using grain oriented silicone steel for the stator teeth is shown to improve torque production of the machine. The wire, coil, and stator geometry are modified to reduce copper loss. A tightly spaced coil, axially centered on the tooth, with high aspect ratio wire and chamfered pole shoe is shown to reduce loss. Finally, a compact stator winding is proposed with coil terminations on the inner diameter of the stator. The proposed winding reduces the volume of the machine, as well as further reducing copper loss due to less wire utilized. These actions significantly improve the efficiency of the machine, while reducing weight and volume.

# Acknowledgements

I would like to first thank my advisors and colleagues at the McMaster Automotive Resource Center (MARC). Thank you to my advisor Dr. Ali Emadi for his guidance and support in my research, as well as for leading this world class research group. Thank you to Dr. Ehab Sayed for his mentorship and guidance throughout my degree. This work would not have been possible without his technical knowledge and advice. I would like to acknowledge Dr. Ehab Sayed, Dr. Giorgio Pietrini, and Dr. Alan Callegaro, for enabling this work and for their leadership of our research team. Thank you to Mohamed Abdalmagid for his contributions in Chapter 5 related to the insulation system. Thank you to all my colleagues in the research team for their excellent work and collaboration, including co-authorship on multiple publications. This research work is team effort.

I would also like to acknowledge the challenges of COVID-19 and the amazing ways that this research group has adapted. Thank you again to my research colleagues, and group leadership, but also the technical support staff at MARC for seamlessly moving us to a virtual work environment. Thanks to their efforts our work progressed.

I would like to acknowledge and thank Eaton Aerospace for their cooperation in and funding of this research project. I am highly appreciative of being able to directly apply my research to a real world application, and be able to share our findings. Additional funding was also provided through the Mitacs Accelerate Program.

Thank you to all my previous colleagues and collaborators at Ford Motor Company and McGill University for their technical teaching, motivation and guidance. Their support has set me on an exciting path working on vehicle electrification.

Finally, thank you to my family and friends who have supported me. My parents and grandparents for their love and support, and pushing me in my education, including sending me off to study in the cold. My family in Canada that have welcomed me. Ali and Emmett for always making talking about work and academia fun. Nadège, merci pour tout. This thesis is dedicated to them.

# Contents

# List of Figures

# List of Tables

# Nomenclature

## Acronyms

| | |
|---|---|
| AF | Axial Flux |
| AFPMSM | Axial Flux Permanent Magnet Synchronous Machine |
| AMM | Amorpheous Magnetic Material |
| Arms | Ampere Root Mean Square |
| BEMF | Back Electromotive Force |
| CoFe | Cobalt Iron |
| CSA | Cross Sectional Area |
| CTE | Coefficient of Thermal Expansion |
| EDM | Electrical Discharge Machining |
| EM | Electromagnetic |
| eVTOL | Electric Vertical Takeoff and Landing |
| FE | Finite Element |
| FFT | Fast Fourier Transform |
| FSCW | Fractional Slot Concentrated Winding |
| GO | Grain-Oriented |

| | |
|---|---|
| HTSM | High-temperature Superconducting Machine |
| ID | Inner Diameter |
| IM | Induction Machine |
| MEA | More Electric Aircraft |
| MEE | More Electric Engine |
| NiFe | Nickel Iron |
| NO | Non-Oriented |
| OD | Outer Diameter |
| PM | Permanent Magnet |
| PMSM | Permanent Magnet Synchronous Machine |
| RF | Radial Flux |
| RFPMSM | Radial Flux Permanent Magnet Synchronous Machine |
| S/G | Starter / Generator |
| SiFe | Silicon Iron |
| SMC | Soft Magnetic Composite |
| SRM | Switched Reluctance Machine |
| UAV | Unmanned Aerial Vehicle |
| WFSM | Wound Field Synchronous Machine |
| YASA | Yokeless and Segmented Armature |

# Symbols

| | |
|---|---|
| $\delta$ | Skin Depth |
| $\rho$ | Resitivity |
| $B$ | Magnetic Flux Density |
| $f$ | Frequency |
| $H$ | Magnetic Field Density |
| $I$ | Current |
| $l_w$ | Total Wire Length |
| $Loss_{AC}$ | AC Copper Loss |
| $Loss_{DC}$ | DC Copper Loss |
| $\mu_o$ | Permeability of Free Space |
| $\mu_r$ | Relative Permeability |

# Declaration of Academic Achievement

I, Cyrille Goldstein, declare that this thesis titled "On the Stator Design of an Axial Flux Permanent Magnet Synchronous Traction Machine for Aerospace Applications", and the work presented in it are my own. I confirm that the following chapters contain my work, and other works used in this thesis are clearly referenced.

Chapter 1: Introduction

Chapter 2: Axial Flux Permanent Magnet Machines in Aerospace Applications

Chapter 3: Stator Magnetic Materials Selection

Chapter 4: Analysis and Reduction of AC Copper Loss

Chapter 5: Design of a Compact Winding Configuration

Note: The electrostatic analysis presented in section 5.4.3 was completed by Mohamed Abdalmagid.

Chapter 6: Conclusion

# Chapter 1

# Introduction

## 1.1 Background and Motivation

Aviation is one of the fastest growing contributors to global emissions. In the period from 2014 to 2018, emissions from global aviation grew by 32 % and now accounts for about 2.5 % of global $CO_2$ emissions [1]. By 2050 the International Civil Aviation Organization (ICAO) expects air travel to triple by 2045, with a somewhere between 2.2 and 3.1 times increased fuel consumption [2]. In the understanding that the world must work to reduce global emissions and limit the effects of climate change, the ICAO has set a goal of 2 % reduction in aviation emissions per year, with technology improvements accounting for about half of this, along with improved operational efficiency and use of sustainable aviation fuel. However, current projections show that this target may not be reached, and only 1.37 % per year is predicted [2]. We must strive to do better, and limit global emissions. While alternatives to air travel should be encouraged, aviation is a necessary industry and growth is inevitable. Technologies that reduce emissions must be further developed. One way of doing this would be to significantly increase aircraft electrification, including fully electric aircraft. Aircraft electrification is

already present in aerospace. In what is referred to as the More Electric Aircraft (MEA) systems and actuators within the aircraft are replaced with electric motors and electric power systems. Doing this reduces the load on the primary propulsive engines, and/or reduces the weight of the aircraft, thereby improving efficiency [3]. Some examples of current MEA are the Boeing 787 and Airbus A350 and A380 [3]. These actions and the progression of MEA technology are taken into account to some degree in the ICAO predictions, but much of the predictions focus on airframe and combustion engine efficiency improvements [4]. A further increase in MEA will help reach ICAO goals.

In terms of electric aircraft, where the main propulsion system is electric, the current state of the art is still in an earlier stage of development. There are multiple flying prototypes for electric aircraft, and a few aircraft ready for commercial operation [5]–[7] These are mostly smaller propeller driven aircraft, suited for regional transport. There are also a few technology demonstrators of hybrid electric propulsion, where the jet or turboprop engine works in parallel with a separate electric propulsion system [8]. At this level of technology, electrification is unlikely to make a major impact on emissions. A 2019 study by the International Council on Clean Transportation identified that $CO_2$ emissions from regional flights only accounted for about 5 % of global aviation emissions, which is dominated by narrow and wide body jets, as well as freight [1]. However, the development of these technologies on small aircraft is a crucial stepping stone to electrifying larger aircraft. Some of the challenges that can be solved at a small scale are the power density of batteries and the electric drive, achieving a level of reliability and fault tolerance suitable for aerospace, and developing engineering standards and a regulatory environment for adoption of widespread electrification. Investment in the development of electric propulsion will enable significant reductions in emissions, at first for local and regional air travel, and then larger aircraft.

The goal of this project is to develop a compact, but high power electric drive system for an all electric aircraft. This is a joint project between the McMaster Automotive Resource Center (MARC) and Eaton Aerospace. One of the objectives is to improve the compactness and power density of the electric machine. The machine type under development is an axial flux permanent magnet machine (AFPMSM) chosen for its high power density and ability to package well in the available space. Chapter 2 discusses the machine choice in further detail. There are many aspects to the project, including the machine design, prototyping of machines, and testing. As will be outlined in the next section, the contribution of this thesis focuses on the stator design of the AFMPMSM. This work helps advance the technology necessary for wide scale electrification of aircraft and enable the necessary emissions reductions of the next decades.

## 1.2 Thesis Contributions

The stator design of an AFPMSM developed for an aerospace application is investigated. Modeling approaches for APMSMs are compared, and a three-dimensional finite element (FE) modeling method is developed. The model takes advantage of machine geometry, symmetry, and meshing to reduce simulation time. Total copper loss is captured using a hybrid method were AC loss is calculated by FE model using a simplified wire geometry, and DC loss is calculated analytically.

A comparative study is completed of soft magnetic materials for the stator teeth. The material properties are analyzed, and core loss data is fit to a loss model within the FE tool. The performance of the machine is captured utilizing different materials for the stator teeth. A grain-oriented electrical steel is proposed as the optimal material.

The origins of copper loss are investigated. The impact of skin effect, proximity effect, and rotor leakage flux are shown in an AFPMSM. Their sensitivity to temperature and fundamental excitation frequency is analyzed. Copper loss is studied across a range of wire sizes and operating conditions, and the optimal wire size is selected. Modifications to the wire and stator geometry are compared for their effectiveness at reducing AC copper loss. Recommendations are provided for the effective ways of reducing AC copper loss be modifying a combination of stator, coil, and conductor geometry. An improved stator design using high aspect ratio wire, and larger chamfered pole shoe is shown to reduce AC copper loss.

A compact winding design is proposed with terminations on the inner diameter (ID) of the machine. A novel configuration is employed with additional half turns for three coils, such that the three phase connection is placed at the outer diameter (OD). Winding constraints and a detailed design methodology are presented. The proposed winding design is analyzed, and it is shown to be more compact than an OD terminated winding, with no electromagnetic consequences due to the additional half turns.

## 1.3 Thesis Outline

In this chapter, the thesis topics are introduced. Motivation is provided for why electrification is necessary in aerospace. Particularly, the contributions towards global emissions from commercial aviation are of concern, and different actions are outlined to reduce these impacts. Electrified propulsion has potential to be one the most significant ways to reduce aerospace emissions, and is being developed at a small scale now, before it can be implemented for larger commercial transportation. Finally, the project is introduced; to design a compact and high power electric drive using an AFPMSM for electric propulsion.

In the first part of Chapter 2, a literature review is presented on electric machines in aerospace, followed by a survey on power density of electric machines in aerospace. Permanent magnet machines, including AFPMSMs are identified as machines of interest for aerospace. In the second part of the chapter electromagnetic, mechanical and thermal design of AFPMSMs are discussed, and the design of the machine under study is presented. Then simulation methods for AFPMSMs are reviewed. Analytical, two-dimensional FE models, and three-dimensional FE models are compared through studying available literature. Three-dimensional FE modeling is chosen, since it is highest accuracy approach. Finally, the simulation method used in this thesis is presented, including methods to reduce the simulation time of a full three-dimensional model.

Chapter 3 compares different soft magnetic materials for use in the stator of the AFPMSM. First a review of soft magnetic materials in aerospace electric machines is presented. Then four materials are selected for further study; a non-oriented silicon iron electrical steel, a grain-oriented silicon iron electrical steel, a cobalt iron electrical steel, and a soft magnetic composite. The material properties and modeling approach are investigated, including special considerations for grain-oriented steel. Finally, a comparative analysis is conducted, and performance and loss results for the different materials are presented. Based on these results, the

grain-oriented electrical steel is chosen as the best material.

In Chapter 4 the copper loss in the machine is analyzed, and methods for reducing AC copper loss are proposed. First a review is conducted on the origins of AC loss, including simplified case studies to illustrate the effects of different loss mechanisms. The dependence of these mechanisms on operating temperature and fundamental excitation frequency is also highlighted. Then, further details are given on the simulation method used to capture AC loss for the full machine. The baseline machine is analyzed capturing total copper loss in the winding. There follows a series of studies on stator modifications that can reduce AC loss.

First the wire size is studied, varying the cross sectional area. The relative contribution of AC versus DC copper loss is analyzed across a range of temperature and frequency operating conditions, showing how the optimal wire size depends on the operating condition of the machine. Then, for the chosen wire size, the wire position in the slot and wire aspect ratio are studied. A high aspect ratio wire is shown to reduce AC loss. Further study is then conducted on the pole shoe geometry, varying the thickness and width, as well as chamfering certain edges of the shoe. A thicker pole shoe with a large chamfer is shown to further reduce AC loss. The chapter concludes with a series of recommendations on how best to reduce AC copper loss, and a final machine design incorporating the most effective measures.

In Chapter 5 the compact winding design is presented, incorporating the modifications to the stator from Chapter 4. First, the packaging of the winding, particularly the end terminations, is discussed for an AFPMSM. Alternative winding types are identified that make their connection on either the inner diameter (ID) or outer diameter (OD) of the stator. The ID terminated winding is hypothesized to be more compact. Then, the constraints on the winding design are identified, including available manufacturing methods, insulation requirements and balancing the phase resistance. A detailed design methodology is described, and the design of the ID terminated winding is presented. This winding is then compared against

an OD terminated winding and shown to be significantly more compact. In order to make the ID terminated winding, additional half turns are required for the coils around three teeth, which can impact the magnetic circuit of the machine. A complete model of the machine is analyzed in terms of electromagnetic performance. The chapter concludes by showing that the ID terminated winding is more compact, with less copper use, and has no negative electromagnetic consequences.

Chapter 6 concludes the thesis. The contributions of preceding chapters are summarized and important points are re-emphasized. The stator of an AFPMSM has been improved by increasing torque production with grain-oriented steel, reducing AC loss by changing the wire and stator geometry, and proposing a compact ID terminated winding design which reduced copper use, overall weight and volume of the machine. This is an important part of the overall project objective to deliver a compact, high power electric drive for an electric aircraft.

# Chapter 2

# Axial Flux Permanent Magnet Machines in Aerospace Applications

## 2.1 Introduction

As an introduction to this research, a literature review focused on electric machines in aerospace is presented. The review focuses on types of electric machines, their applications in aircraft, and concludes with a study of achievable power density. The AFPMSM is identified as a very competitive machine choice for electric propulsion where high power density is key. Following this review, an overview is presented of the design of AFPMSMs and specifically the AFPMSM developed in this project. Electromagnetic, mechanical, and thermal design is discussed. This section gives the necessary background for the further studies that make up the primary contributions of this work. Finally, modeling methodology of an AFPMSM is introduced. The methods presented here are used throughout this work to assess the proposed design improvements.

## 2.2 Review of Electric Machines in Aerospace

Electric machines are used in many different systems and mechanisms in aerospace. Their use is also not new, since the 1940's electric motors and actuators have been employed in aircraft [9]. However, in recent years the concept of the MEA has become highly prevalent [3], [9], [10]. MEA refers to electrification of auxiliary power systems in aircraft. This can include replacing pneumatic systems, like de-icing, aircraft pressurization and air conditioning, and hydraulic systems, like flight controls and landing gear [3]. There is also a subset of MEA referred to as More Electric Engines (MEE) which seeks to integrate electric machines for engine start, and auxiliary power generation, within the engine, as opposed to an external machine linked with a gearbox [3]. By integrating these systems into a single infrastructure of electro-mechanical systems, there can be significant improvements in efficiency and reliability [3]. Many in production aircraft today are highly electrified, for example the Boeing 787 and Airbus A350 [3].

In addition to the concept of MEA, more efforts are being made to fully electrify primary propulsive power in aircraft. Currently this is most widely seen in smaller scale applications, like unmanned aerial vehicles (UAVs), single engine propeller aircraft, or electric vertical take-off and landing aircraft (eVTOL) [5], [11]. The key enabler for electric propulsion in aerospace is the volumetric and gravimetric power density of electric propulsion systems. As battery energy density improves as well as innovation in high power density motors and inverters, larger aircraft will be electrified. Electrification in aerospace is one of the most exciting areas of interest in aerospace research, and will only become more important as the need to improve aircraft efficiency becomes more urgent.

In terms of machine design, almost every type of electric machine can be found employed in aerospace applications. However, the requirements for electric machines in aerospace tend to vary from those in other applications, like automotive or general industry. For example, fault tolerance and reliability are often cited as

key requirements, as well as tolerance of temperature extremes, both and high and low. Of course, power density and overall weight of the machine can not be ignored. Both radial flux (RF) and axial flux (AF) machines have been researched. Machine types include permanent magnet synchronous machines (PMSM), switched reluctance machines (SRM), wound field synchronous machines (WFSM), induction machines (IM), and in certain propulsion applications, high temperature superconducting machines (HTSM).

This section will discuss the different types of machines used in aircraft electrification today. This is broadly divided into machines for MEA versus propulsive machines. Finally, power density of machines in aerospace is studied, and a survey is conducted to assess the power densities achievable today.

### 2.2.1 Electric Machines in MEA

Pneumatic systems are heavily used in conventional aircraft. Eliminating this load on the engine can significantly improve the turbine efficiency [3]. The Boeing 787 almost entirely reduced the use of pneumatics by replacing de-icing, air conditioning, hydraulic pumps, and engine start with electric machines and variable frequency drives. This change allowed for a 1-2% reduction in fuel burn in cruising conditions, reduced aircraft weight, and improved reliability and maintenance intervals due to simpler systems [12]. In another example just the air conditioning load was replaced, which is significant for a large aircraft. In [13], a 100 kW RFPMSM was proposed for air conditioning in an MEA, with a focus on very high speed operation in order to further improve efficiency of the air conditioning compressor.

Flight controls and landing gear are generally hydraulic systems in conventional aircraft. By replacing these controls with electric actuators, overall system weight and complexity can be reduced. Additionally, maintenance is simplified, and reliability can be improved [3], [14]–[16]. There is considerable current re-

search on electric machines for replacing hydraulic systems. In [17] and [18] two approaches were presented for nose wheel steering mechanisms. [17] studied a 5 phase RFPMSM, with emphasis on reliability due to the multi-phase winding. [18] proposed a PM assisted SRM with a dual three-phase interleaved winding. The SRM topology was selected for its superior robustness and fault tolerance, but it was found necessary to add the magnet assist in order to meet the torque requirement. However, the magnet assist concept does not compromise fault tolerance, as the machine behaved as an SRM in open circuit or short circuit fault condition, with low induced current and voltage in the winding. In [19] a five phase SRM was designed for control surface actuation. Again, an SRM was chosen for its fault tolerance, though it was acknowledged to be less power dense. In [20] it was suggested that in actuator applications, a PMSM is preferred for its inherent power density, and the design focus should be on methods for improving PMSMs fault tolerance. This was seen in [21], which presented a PMSM design for control surface actuation with a high pole and slot count fractional winding. The machine topology allowed for a large inner diameter region in which to package the ball screw in order to translate rotary to linear motion. As well, the concentrated wound teeth allowed for good magnetic and physical separation of the winding, improving reliability.

For starter/generators (S/G) integrated in a MEE, the option of a PMSM is less clear, primarily because of the high temperature and high-speed operating condition. In [22] and [23] an SRM machine was studied for S/G applications. In both studies the robustness of the rotor structure was identified as a major factor in the SRMs suitability for the application. The rotor structure was mechanically stronger, since it didn't need to retain magnets or manage stress in thin magnet bridges, while the lack of magnets eliminated the risk of demagnetization. Additionally, the inherent fault tolerance of an SRM was beneficial [22]. This was also cited in [24],[25] and [26], where IMs are proposed for a S/G. Like in an SRM, an IM has better fault tolerance due to the lack of Back Electromotive Force (BEMF)

in the fault condition, and no concerns over magnet demagnetization. As well, the ease of field weakening operation with an IM is beneficial for the very high-speed operating conditions [25]. There has been some development of PMSMs for starter generator applications, including in [63] and by the University of Sheffield in partnership with Rolls Royce [39], though there are not many published details on how these manage the temperature and stress loads of the application. Within the aerospace industry, the current most common machine type for a S/G is the WFSM [27]. This is the type of machine in the Boeing 787, a highly MEA. The WFSM is favored for its complete field control, and therefore good fault tolerance, as well as simple control, flexibility in architecture, and robust structure [27]. In short, it is very well proven technology that is reliable for aerospace applications. However, power density is generally lower than SRMs or PMSMs, though a recently demonstrated WFSM from Honeywell seems to match state of the art PMSMs [27].

### 2.2.2 Electric Machines for Electric Propulsion in Aerospace

In electric propulsion, power density, and high continuous power levels are of primary importance. There has been much study around PMSMs and HTSMs for propulsion applications, generally for propeller driven aircraft or rotorcraft. In [39] multiple PMSMs were studied that have been developed in industry for propulsion. Siemens developed three machines, all RFPMSMs with surface mounted magnets with power density between 5 and 7 kW/kg continuous. Rotex developed a 50 kW machine for small aircraft, with surface mounted magnets in an outer rotor RFPMSM. They achieved 4 kW/kg. One of the first operational commercial electric aircraft to take flight used a RFPMSM developed by MagniX [6]. This machine had a power density of 4.2 kW/kg continuous [28]. There has also been development in AFPMSMs for propulsion, with one of the better known being machines from Enstroj, designed for the gliders and small aircraft. They achieved

power density of 4.9 kW/kg continuous, though at peak power, this approached 10 kW/kg. Yasa has also developed an AFPMSM to be used in a prototype electric aircraft developed by Rolls-Royce [7].

HTSMs cryogenically cool the machine, reducing the operating temperature of the machine to 20 to 60K (around -230 °C) and employ high temperature superconducting conductors, or high conductivity copper or aluminum windings [29]. At these temperatures, the resistance is extremely low, and current density, and consequently magnetic flux density in the machine, is greatly increased. HTSMs have been investigated by NASA for their goal of pollution free flight [29]. When comparing HTSMs to other machines it is important to consider the weight of the cooling apparatus, but even then, power density in the range 6-7 kW/kg is possible, which approaches the power density of combustion turbine engines [29]–[33]. Another possibility with HTSMs is to use cooled liquid hydrogen as a fuel cell energy source, where the liquid hydrogen must be warmed up before use. The liquid hydrogen can be warmed by using it as a coolant in an HTSM, thereby giving a "free" source of coolant [30], [32].

### 2.2.3 Power Density in Electric Machines for Aerospace

The previous discussions focused on identifying machine choices for different applications in MEA and electric propulsion. For all applications a key metric for the machine is power density. This was discussed in the context of propulsive machines, but is also important for machines employed in MEA. Fig. 2.1 presents the continuous power density for a range of machine types, for different applications, developed both in academia and industry [26]–[28], [31]–[41]. All the machines cited here are a complete design, where the power density considers the weight of the motor housing, shafting, and cooling system, not just EM weight. The power density of HTSMs includes the weight of any chillers required for operation. Most of these machines are either in production or have been prototyped. Many

other theoretical studies for aerospace machines are present in the literature, but they either don't calculate the machine weight or only calculate the weight of electromagnetic materials.

Studying the figure, AFPMSMs, RFPMSMs and HTSMs tend to have the highest power density. Though WFSMs, SRMs and IMs are often cited in literature as a good choice for their robustness in aerospace applications, it doesn't appear that the current state of the art matches the power density possible with PM or HTS machines. A notable exception is the previously discussed WFSM developed by Honeywell claiming 7.9 kW/kg, though not much is known about this machine. RFPMSMs have been most extensively investigated, though this does not necessarily reflect the number of applications currently in commercial use. As mentioned, WFSMs are more common in aviation today. The overall picture is of an industry and research groups transitioning towards more PM machines for aerospace.

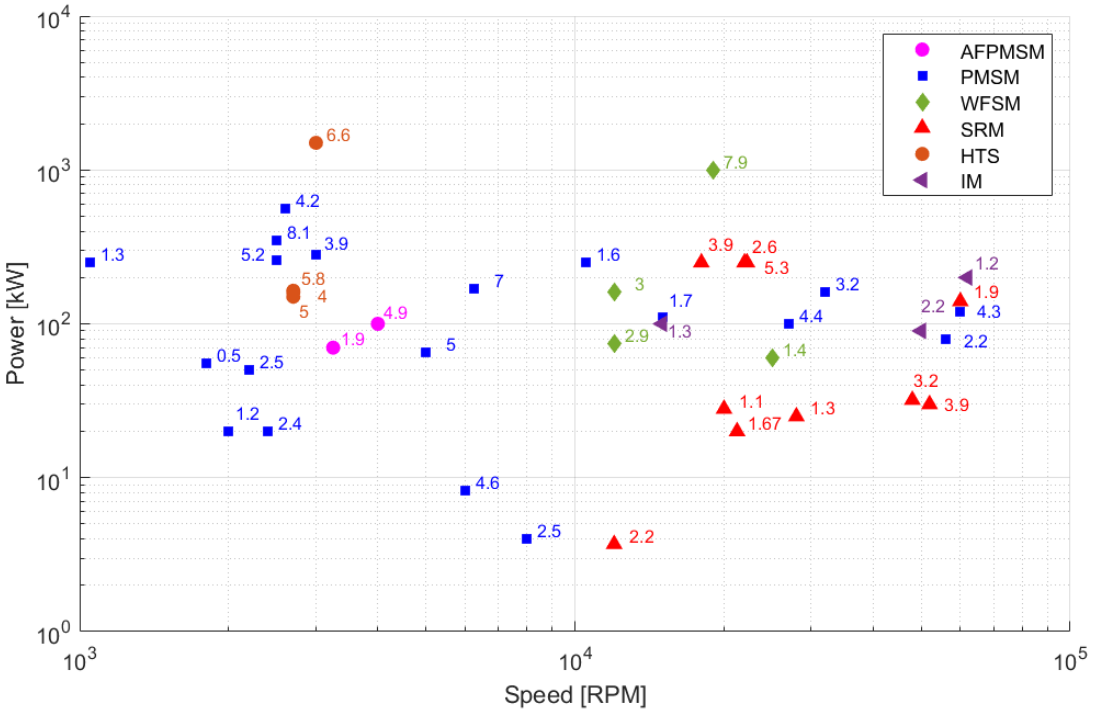


Figure 2.1: The continuous power density [kW/kg] for different types of electric machines in aerospace applications.

## 2.3 Design of an AFPMSM

### 2.3.1 Electromagnetic Design

There are multiple types of AFPMSMs that have been developed. The first classification that must be made is the configuration and number of rotors for each stator assembly. While radial flux machines commonly have a single rotor and a single stator, an axial flux machine can have a single rotor and single stator, two stators and one rotor, or two rotors and one stator. The two-rotor single stator torus design may have further variation in the alignment of the rotors and stator. The rotors can either be magnetically aligned with each other, the so-called north-south (N-S) arrangement, creating one large flux loop from one rotor through the stator to the opposing rotor, or symmetric (N-N) where the flux loop is contained

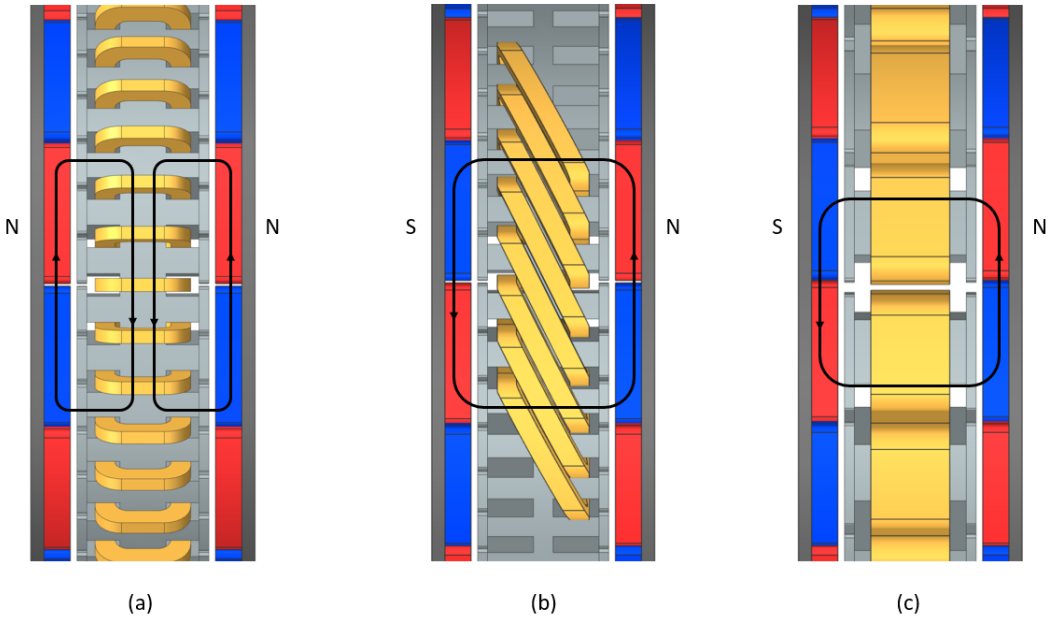


Figure 2.2: The NN-Torus (a), NS-Torus (b) and YASA (c) configuration of an AFPMSM.

within the stator and symmetric through each rotor (Fig. 2.2)[42]. The N-S has a better power density, but is disadvantageous with respect to packaging, requiring more winding connections to form a lap winding, and has large end windings. The N-N winding is easier to wind but requires a large stator yoke. Woolmer and McCulloch propose an alternative topology, with the same magnet layout as the N-S design, but removing the stator yoke, and increasing the pitch of the tooth in order to use a concentrated winding instead of a lap winding [42]. This is the yokeless and segmented armature (YASA) design. This has been found to improve power density and is easy to wind, with compact end windings. Some aspects of manufacturing are more complex however, because the stator teeth are now floating in space and must be secured with high strength, but non-magnetic material [42]. As has been stated, power density is a key performance metric for aerospace projects, hence the YASA design is chosen for this project. The different AFPMSM configurations are illustrated in Fig. 2.2, with limited coils shown for the NS-Torus configuration, such that the stator yoke is visible even with the winding.

Having chosen the high-level topology, the number of stator slots and rotor poles as well as winding configuration should be defined. The YASA machine employs a fractional slot concentrated winding (FSCW). In this type of winding either every tooth is wound, or every other tooth is wound, which creates either two winding layers in the slot (double layer), or a single winding layer in the slot (single layer). Literature has shown that the double layer winding reduces harmonics in the machine, and increases performance [43], [44]. The slot/pole combination should be chosen to have a high fundamental winding factor. However, it also impacts many other electromagnetic aspects of the design, such as the fundamental excitation frequency, torque production, harmonic content, torque ripple, losses, and flux density in the teeth [43], [45]. As well, there are practical considerations depending on the intended diameter of the machine versus number of slots and poles. A large diameter machine with few slots would require complex tooth shapes. Table 2.1 shows the winding factor for a few common slot/pole combinations with a double layer winding [46].

Table 2.1: The Winding Factor of Common Slot/Pole Combinations

| No. of Slots \ No. of Poles | 10 | 14 | 16 | 20 | 22 |
|---|---|---|---|---|---|
| 12 | 0.966 | 0.966 | 0.866 | | |
| 15 | 0.866 | 0.951 | 0.951 | 0.866 | |
| 18 | | 0.902 | **0.945** | 0.945 | 0.902 |
| 21 | | 0.866 | 0.890 | 0.953 | 0.953 |
| 24 | | | 0.866 | 0.966 | 0.958 |

For the machine under study, the 18-slot 16-pole combination was chosen. The combination has a high winding factor, good torque density due to the high pole count, and low losses. The 24/20 winding was found to have better torque density but higher losses, particularly AC copper loss, due to the increased fundamental excitation frequency. The 12/10 combination has lower core loss but also lower torque density.

In finalizing the high-level winding design, the number of coil turns is selected based on balancing the voltage limit of the machine, with the desired current level and the wire cross section. Further details on the winding design, wire size, and how they impact copper loss and packaging are presented in chapters 4 and 5.

Finally, the stator and rotor geometry must be defined. The stator tooth geometry is chosen to limit saturation due to high flux, and achieve good torque capability, while limiting weight. Core losses should also be minimized and the tooth geometry should not constrain the winding. A larger tooth may increase torque and reduce saturation, but limits the slot width, increases weight, causes the coil diameter to increase which increases copper losses, and may impact core loss. Hence, the tooth size is generally made large enough that flux levels are kept below the saturation limit, but not larger. Tooth tips or shoes, as well as wedges in the slot opening may be added to better control flux paths, improve torque and

limit losses. As well, the magnetic materials in the stator must be defined, and this will be studied in chapter 3.

The rotor balances similar issues, torque should be maximized, without increased loss. Here a multi-segment Halbach array is employed with N48 grade permanent magnets to maximize torque production and reduce the need for a large back iron. The Halbach array also reduces harmonics in the airgap flux, which reduces stator losses. The rotor magnets are also segmented in order to reduce eddy current losses, while still having a large magnet volume. Eddy current losses due to the harmonic content of FSCWs is a common issue [47].

### 2.3.2 Mechanical Design

Having defined the electromagnetic configuration, those components must be supported in a structure that can resist both the electromagnetic and external forces on the machine. As mentioned, the YASA design presents some complexity because the stator teeth are floating in space and not connected by a stator yoke. In order to maintain the stator structure, the stator teeth and winding are potted with a plastic encapsulant. This is a multi-step process where individual teeth are potted and then aligned in place for a final potting process. The ID of the stator holds a bearing carrier, upon which the main rotor bearings sit. The OD of the stator is a metallic stator housing, which also integrates a water jacket for cooling, and main mounting bolts for the machine, evenly distributed around the perimeter. The bearing carrier and stator housing are manufactured out of aluminum since it is both non-magnetic, high-strength and low weight.

In this design, one of the key aspects is ensured reliable torque transfer between the stator housing, the plastic encapsulant and the stator teeth. While in a nominal condition the adhesive properties of the plastic encapsulant ensures the integrity of this joint, this must be ensured across a range of temperatures, and over time. Hence, it is important to consider the varying coefficients of thermal

expansion (CTE) of the different components. In this case the aluminum stator carrier has much higher CTE than the iron stator teeth. The plastic encapsulant is modified by the addition of fillers that modify the CTE such that it is between that of aluminum and iron. This reduces the stress due to mismatched CTE over changing temperature. As a further measure, keys or teeth can be molded into the encapsulant that "lock" into the stator housing.

The rotor structure must resist the rotational forces causing centripetal stress in the rotor, the magnetic forces that pull the magnets towards the stator, and transfer the torque from the magnets to the output shaft. The magnets and magnet back iron are supported by a rotor carrier. The magnets and back iron are glued in place with a high strength epoxy. The rotor carrier can be made of high strength non-magnetic materials, like aluminum, stainless steel, or titanium. The rotor carrier is bolted to the main rotor shaft, which spins on bearings inside the bearing carrier of the stator. The alignment between rotors on either side of the stator is critical to maintain expected electromagnetic performance. A high precision key is used for this purpose.

An exploded view of the machine assembly, with important components labeled, is shown in Fig. 2.3. Note that the coils and winding are not shown in detail, as their design will be discussed further in later chapters. The stator encapsulant is also not shown, in order that other components are visible.

.

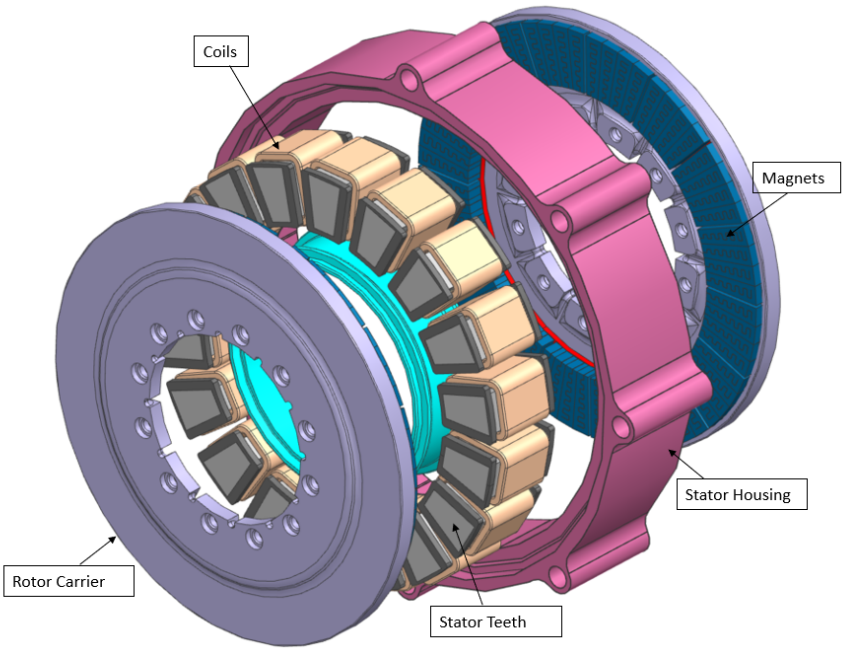


Figure 2.3: The machine under study.

### 2.3.3 Thermal Design

A thermal management system is necessary to maintain performance of the machine under high loads. The efficacy of the cooling system is the main factor in setting the continuous power limit of the machine. In this machine, both the rotor and stator are cooled. The stator is cooled with a water jacket in the housing, plus a series of cooling channels in the slots between coils. The cooling channels are formed as part of the plastic encapsulation. A mold in the shape of the cooling channel is left in place during the encapsulation process, then removed, leaving a void in the shape of a thin cross section channel that passes by each coil. This system forces the fluid in the water jacket to flow directly past the coils, greatly increasing cooling performance. As well, the same fillers that modify the CTE of the plastic encapsulant serve to improve the thermal conductivity, allowing greater heat flow from the coils to the cooling channels. Aluminum oxide is a common choice of filler because it has high thermal conductivity but is non-magnetic and non-conductive. The water cooling circuit of the stator is also shared with the

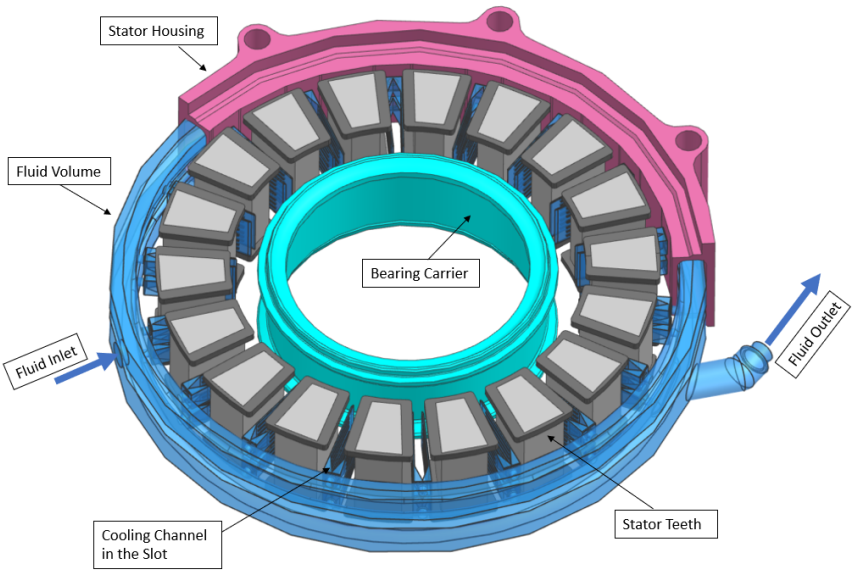


Figure 2.4: The stator cooling system.

drive inverter, so there is no extra cooling hardware required for the motor. The stator cooling system is shown in Fig. 2.4. The shape of the fluid volume is shown in the transparent blue.

The rotor cooling is purely convective in nature. The magnets are cooled by forcing air through the airgap, and over the back of the rotor carrier. This is improved by ducting and fins around the machine in order to direct and increase airflow over hot spots. There is significant discussion in literature about the benefit of convective cooling with air versus a liquid medium like oil. In a previous review of electric drives in aerospace, it was found that air cooling is prevalent for medium power propulsion machines in the range of 10 to 100 kW, where the electric machine is exposed to outside airflow [34]. However, in [37] air cooling was compared with oil cooling for a generator for a MEA, and it is found that the oil cooled machine had a 30 % higher power density due to improved cooling. Here, air cooling is chosen because of its significantly simpler, and more robust implementation. To implement oil cooling would require an additional pump and oil cooler, which adds complexity and weight. This is common in aerospace applications, because of the importance placed on reliability [29], [34], [48].

## 2.4 Simulation Methods for an AFPMSM

This section introduces modeling approaches for AFPMSMs. Due to the three-dimensional nature of an AFPMSM a common approach for simulating a RFPMSM with a two dimensional axial slice of the machine is not possible. Hence multiple alternatives have been proposed. These include analytical models, two-dimensional models with multiple slices, three-dimensional models, and hybrid models combining these approaches [49]–[56]. While these different approaches have all shown reasonable accuracy in terms of torque, this work requires accurately capturing losses within the machine, particularly AC copper losses, which requires calculating three-dimensional current density fields within conductors.

Analytical models proposed in [52], [53], or evaluated in [55], had low simulation times, in the order of minutes, but lacked the necessary accuracy in capturing AC copper loss. To improve the accuracy, 2D FE models are often used, and this has a wide range of applicability for radial flux machines since they can be well represented as 2D slices. Additional analytical elements can be added to account for losses in the end windings or other 3D effects [51]. However, AFPMSMs have a three-dimensional geometry and a 2D simulation is less able to capture the machine behavior, particularly current concentrations that vary from the inner diameter (ID) to the outer diameter (OD) of the slot. Several methods have been proposed to improve this approach by using multiple 2D simulations across evenly spaced cut planes, and certain methods do address AC copper loss simulation [49], [54]. These studies see reasonable accuracy, in the range of 10 %.

For better results, a full 3D simulation is the most accurate, but very computationally intensive [49]. Different methods can be employed to reduce the FE model size such as taking advantage of model symmetry or increasing the conductor mesh density only in the areas of greatest AC loss [49], [55]. With the increased computing power available today, some more recent studies directly employed 3D FE models for the best accuracy [50], [56]. In [55] a hybrid model was proposed

using a simplified 3D FE model to quickly capture the flux density throughout the slot, and then analytically calculate the AC copper loss. This method saw good accuracy but is limited to conductor diameters where the flux density can be assumed constant within the conductor, which is not the case here.

Based on the need for high accuracy, a 3D FE model will be employed. However, the computation time can be problematic. Multiple actions are taken to reduce the model size, without sacrificing model accuracy. The machine periodicity and symmetry are taken advantage of by splitting the machine into a 180° segment, and then splitting the machine axially with a natural boundary condition. The final model is a one quarter model. As well, in studies where AC copper losses do not need to be captured, the coil conductors are modeled as a single bulk conductor with a defined number of turns. This reduces the total element number by close to 50 %. Then in studies where AC losses are captured, conductors are modeled, but mesh density is focused on the airgap, so as to limit element numbers in areas of low losses. The model with bulk conductors is shown in Fig. 2.5 The model to capture AC losses will be re-introduced in chapter 4. Finally, access to a high-performance computation (HPC) server has allowed for running larger models with relative ease. This server has up to 32 processors and more than 300 GB of memory.

## 2.5 Chapter Summary

This chapter presented a review of aircraft electrification, identifying trends in MEA, and electric propulsion of aircraft. Then the different types of electric machines found in aerospace were introduced and compared. Particularly, unique requirements for aerospace were discussed. For instance, the need for fault tolerance, or robustness in high temperature environments, and how machines are designed to accommodate these requirements. As well, certain machines make more sense for particular applications. For instance, SRMs while lower in power

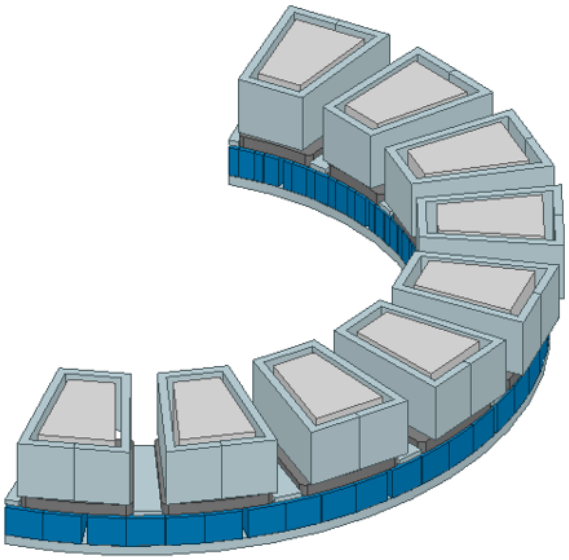

Figure 2.5: The FE model of the reference machine.

density than PMSMs, seem promising for integrated starter/generators operating in high speed, high temperature environments, since the simple rotor structure without permanent magnets is very robust. For all applications, power density is one of the key requirements. To this end, a survey of power density of electric machines in aerospace was conducted. It was identified that RFPMSM, AFPMSM and HTS machines have the best performance for this metric.

This project focuses on the development of an AFPMSM for a propulsion application. Hence, the high level electromagnetic, mechanical, and thermal design of AFPMSMs was introduced. In the process, the design of the machine under study was presented. Finally, FE modeling of AFPMSMs was discussed. While alternative, less computationally intense methods were studied in the literature, three-dimensional FE was selected as the primary modeling method for this work. This is because the ability to accurately capture losses, particularly AC copper loss, is required. The next chapters will present the main contributions of this work: magnetic material selection in the stator, AC copper loss reduction, and a compact winding design to improve power density.

# Chapter 3

# Stator Magnetic Materials Selection

## 3.1 Introduction

Material choice is an important consideration in the stator design of an AFPMSM. Factors to consider include the performance, cost, and manufacturing constraints. This chapter will focus on the material choice for the stator teeth of the considered YASA type machine. In YASA machines, the stator teeth are separate in the stator, as opposed to machines with a yoke. As well, many machines employ a tooth with a pole shoe that partially covers the coil. This can be all one part, or multiple, and the shoe may be a different material than the tooth [42], [57]–[59]. Finally, some machines employ slot wedges in the slot opening to help control leakage flux paths in the machine, and reduce permanent magnet losses due to slotting effect [60]. The components of the stator are identified in Fig. 3.1.

This chapter begins with a review of soft magnetic materials in the stator, looking at trends in material selection for aerospace machines. Then, four candidate materials are selected for the stator, a grain-oriented silicon iron (GO-SiFe) steel, a non-oriented silicon iron (NO-SiFe) steel, a cobalt iron (CoFe) steel and a soft

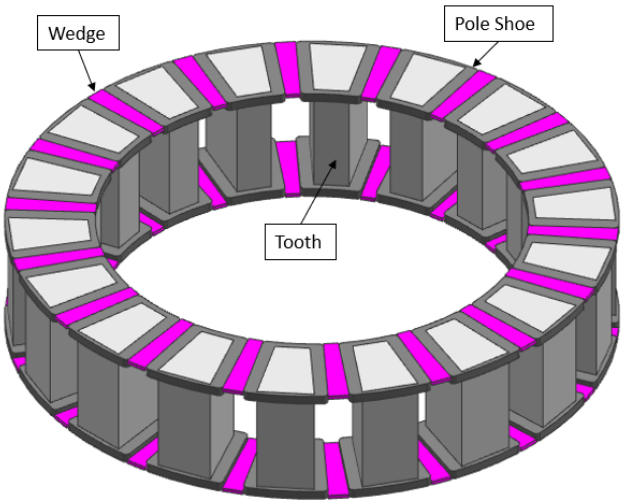


Figure 3.1: The stator tooth, pole shoe, and wedge assembly.

magnetic composite (SMC). A study is defined using these four materials for the stator tooth, and SMC for the pole shoe. Modeling of these materials is studied, and the material properties and manufacturing considerations are compared. Finally, the performance results with these different materials are obtained, and a recommendation is made for the optimal material choice.

## 3.2 Review of Soft Magnetic Materials in the Stator of an AFPMSM

Either laminated electrical steels or SMCs could be used for the stator teeth in an AFPMSM. The most common are NO-SiFe steels [61]. NO refers to the grain structure. All electrical steels are rolled into thin sheets, but the rolling and heat treatment processes undergone will affect the grain structure of the steel. NO steel is manufactured such that the magnetic and mechanical properties of the material are isotropic regardless of the magnetic flux orientation in the material [62], [63]. This is opposed to grain-oriented (GO) electrical steels, where the magnetic and mechanical properties are optimized along the grain direction. As such, the magnetic performance of the material is usually better than NO steel

along the grain direction, but worse across the grain direction. NO-SiFe is very common in radial flux machines, due to the rotating nature of the flux field in the stator. However, in YASA axial flux machines, GO-SiFe is of interest because the flux field orientation is very aligned within the tooth [63], [64]. This is especially true for multi-part stator teeth with a separate shoe. The shoe can be made of material more tolerant to varying orientation flux fields. In [63], an AFPMSM was proposed with GO steel for the stator cores, which saw a 10 % increase in torque, and reduction in losses as compared to a similar design in NO steel. In [64], a similar comparison was carried out, but on an AF switched reluctance machine. Further work was undertaken to optimize the steel grain direction relative to the axis of the tooth to best match the flux path, which in this case was not perfectly axially aligned with the tooth. They were able to achieve a 20% increase in torque as compared to the same machine with NO steel [64]. Available commercially, Magnax AFPMSMs designed for automotive applications also use GO steel [58].

As well as the grain orientation, SiFe steels can vary in silicon content. Most commercially available SiFe steels contain between 1-3% silicon [61]. There have also been some high silicon steels developed, with 6.5% silicon content. These are commercially available for NO-SiFe [65], and there has been research for high Si GO-SiFe steels [66], [67]. For both types of steel, losses improve with higher Si content, but permeability and maximum flux density are reduced [61].

Iron can also be alloyed with cobalt to form CoFe electrical steel [61]. CoFe steel generally has the highest saturation flux density among soft magnetic materials, reaching as high as 2.4 T, with good permeability, and low core losses [61]. CoFe has a high curie temperature, allowing high temperature operation. Moreover, mechanical strength can be very good, though is a function of the material annealing process, with a tradeoff being made between better mechanical versus magnetic properties [68]. The cobalt percentage varies between 15 % and 50 % cobalt, with 48-50 % being the most common, and seeing the greatest benefit in terms of performance. The main drawback of CoFe is its high cost and the rarity of

cobalt [61], [68]. Hence, CoFe is primarily used for aerospace, motorsports or other high-performance applications where high power-density is key. In [24], CoFe and SiFe were compared in an induction machine for a starter generator in a MEE. It was found that even though the CoFe material is denser, 8120 kg/m3, than the SiFe, 7650 kg/m3, the CoFe design was 11.22 % lighter taking advantage of the higher saturation level. Additionally, it was found that by replacing the rotor laminations with CoFe instead of SiFe, total iron losses are reduced by 7 % [24]. In [23], Hiperco 50HS, a CoFe steek heat treated for high mechanical strength, was chosen over SiFe for an SRM machine for an MEE application. They noted that while CoFe was significantly more expensive than SiFe, it was preferred for MEE applications where the electric machine is in the high-pressure region of the engine, where it experiences high temperatures.

Finally, two other laminated steels should be mentioned, they are amorphous magnetic material (AAM), and nickel iron steel (NiFe). AMM is extremely thin sheets (25-30 $\mu$m) of steel, heat treated in such a way as to create an amorphous (disordered) crystal state. The resultant material has very low hysteresis and eddy current losses [38]. However, the material has a lower saturation level, and is difficult to manufacture [38]. In [38] and [13], AMM was used in the stator and rotor cores of very high-speed machines in aerospace (60,000 rpm and 300,000 rpm, respectively) since it has low losses at high frequencies. In terms of axial flux machines, there have been some applications of AAM, but not in aerospace [69]. NiFe has a nickel content of 40-50%, giving it very high permeability, and like AAM, is also typically employed for lower machine losses. It has a lower maximum flux density, which limits its applicability for high power applications [61]. In [70], NiFe, SiFe, and CoFe were considered for 30,000 rpm SRM, with an operating temperature of 200 °C for a MEE application. However, NiFe material was not found to be suitable for the application due to its low saturation level and low curie temperature despite its exceptionally high permeability.

As opposed to the previously discussed laminated steel materials, SMCs are a homogeneous composite material made up of iron powder compressed in an insulating matrix material. SMC has good manufacturing flexibility; it is particularly useful in machine designs with 3D flux paths or where the shape of the core is difficult to achieve with stacked laminations [61]. It is also relatively low cost. However, the low mechanical strength and low saturation level can be major drawbacks [61]. In terms of losses, it has low eddy-current losses due to its high resistivity, which is beneficial at high frequency [61], though hysteresis losses are high at low frequency [57]. Many AFPMSMs have been developed using SMC for the stator teeth, and/or shoes [42], [57], [71], [72]. In [71], SMC was used for the stator bars of an axial flux machine for electric taxiing, because of its lower core loss at medium to high frequencies, the 3D flux paths in the stator, and its easy of manufacturing. In [72], SMC was compared against SiFe electrical steel for the stator teeth of an AFPMSM. While torque output was reduced across the speed range, core loss and eddy current loss were lower at high frequency.

## 3.3 Comparative Study of Soft Magnetic Materials in an AFPMSM

### 3.3.1 Materials Under Study

While many different materials have been studied in the literature for AFPMSMs, this work will focus on four more common soft magnetic materials, that were also available for this project. They are Vacuumschmelze Vacodur 49 210 MPa CoFe steel, Cogent NO20 NO-SiFe Steel, Cogent M80-23P GO-SiFe Steel, and Hagonas Somaloy 700HR 5P 800MPa SMC. The CoFe and NO-SiFe steel are 0.2mm lamination thickness, and the GO-SiFe is 0.23mm lamination thickness. This section will discuss what materials are employed in the stator, the material composition, and the material models for the FE simulation.

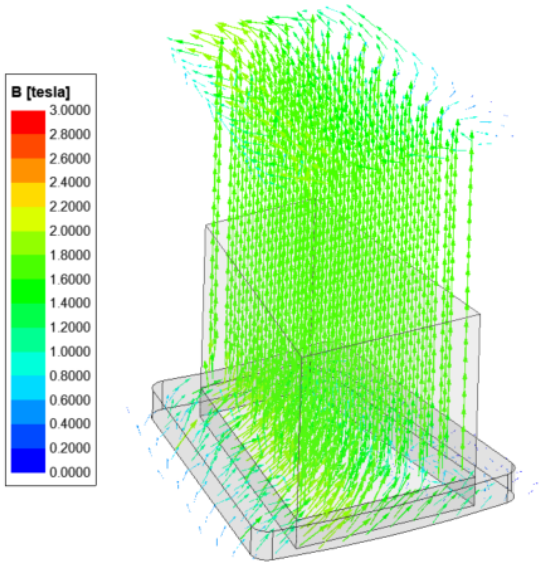


Figure 3.2: The flux vector distribution in a single tooth and pole shoe.

In the stator, the magnetic components are the teeth and the pole shoes. There is also a magnetic wedge between pole shoes that serves to guide leakage flux between the rotor and stator, and reduce slotting effect. This reduces eddy current losses in the winding, and in the magnets. The wedge material considered here is called Magnoval, which is a type of SMC with reasonable magnetic permeability, but very high resistance. It will not be further investigated in the context of the stator materials. The stator teeth, pole shoes, and wedges are shown in Fig. 3.1.

The pole shoe is designed to be manufactured using an SMC material. The complex shape and thin cross section are not easily manufactured with a laminated steel material. Additionally, the flux paths in the pole shoe are three-dimensional, as can be seen in Fig. 3.2, where the flux vector distribution is plotted. A pole shoe and half of the tooth is depicted for geometry reference. The isotropic magnetic nature of SMC is well suited for three-dimensional flux paths.

For the stator tooth, the flux path is much more uniform, so laminated steels are of interest, though the SMC material will also be studied. Multiple studies in literature have identified the opportunity to use GO steels for YASA type AF-

PMSMs due to the uniform flux field orientation in the bulk of the tooth [63], [64]. In Fig. 3.2, we see that in the stator tooth itself, the flux lines are aligned along the axial length of the tooth. A GO steel can be used with with its grain direction oriented axially. CoFe is of interest because of its high saturation level and high induction, with low core loss. It has been deduced in [23], [24] that it can be used to increase torque and reduce losses in the machine. Finally, NO-SiFe is studied as a reference since it is the most common electrical steel used in electric machines, has good magnetic performance, and is very affordable.

### 3.3.2 Modeling of Soft Magnetic Materials

Before comparing the different magnetic materials for the stator teeth, the modeling method for soft magnetic materials is discussed, including dealing with the more complex case of anisotropic laminated electric steel, like the GO steel under study. All materials are modeled with a non-linear $B-H$ curve, considering saturation limits of the material. For the laminated materials, a stacking factor of 0.96 is assumed for the steels under study. Core loss data is supplied by the manufacturers with experimentally gathered loss curves of loss density (W/kg) for varying levels of magnetic flux saturation ($B$) at increasing frequency, from 50 Hz to a minimum of 2000 Hz. Within the FE tool, in this case ANSYS Maxwell, a core loss model is defined by eqn. 3.1 for power loss in terms of coefficients $k_h, k_c$, and $k_e$, for hysteresis loss, eddy current loss, and excess loss, respectively [73]. Where $P_v$ represents power loss in the considered volume, $P_h, P_c$, and $P_e$ represent power loss due to hysteresis, eddy current, and excess loss, and $f$ and $B_m$ represent frequency and magnet flux density. The coefficients $k_h, k_c$, and $k_e$ are defined in an error minimization process. This error is defined as $P_{ij}(experimental) - P_{ij}(k_h, k_c, k_e)$ where $P_{ij}$ is the power loss at flux density $i$ and frequency $j$ [74]. This is in effect a curve fitting process to fit the core loss model to the supplier provided loss curves with the minimum error.

$$P_v = P_h + P_c + P_e = k_h f \beta_m^2 + k_c (f\beta_m)^2 + k_e (f\beta_m)^{1.5} \tag{3.1}$$

For modeling GO steels, further material data and a modified model is required [75]. GO steel has an easy magnetization direction along 0°, or aligned with the grain direction, an intermediate magnetization direction along 90°, and a hard magnetization along 55° [76]. The degree of this effect is also dependent on the flux density level $B$ in the material [76]. This can be seen in Fig. 3.3, where the GO-SiFe relative permeability is plotted versus flux orientation, at two flux density levels. In the FE software, the anisotropic behavior for all flux orientations is calculated based on the 0° and 90° material data according to the model cited in [75]. The necessary data for this model comprises $B - H$ curves and loss vs flux vs frequency curves at 0° and 90°.

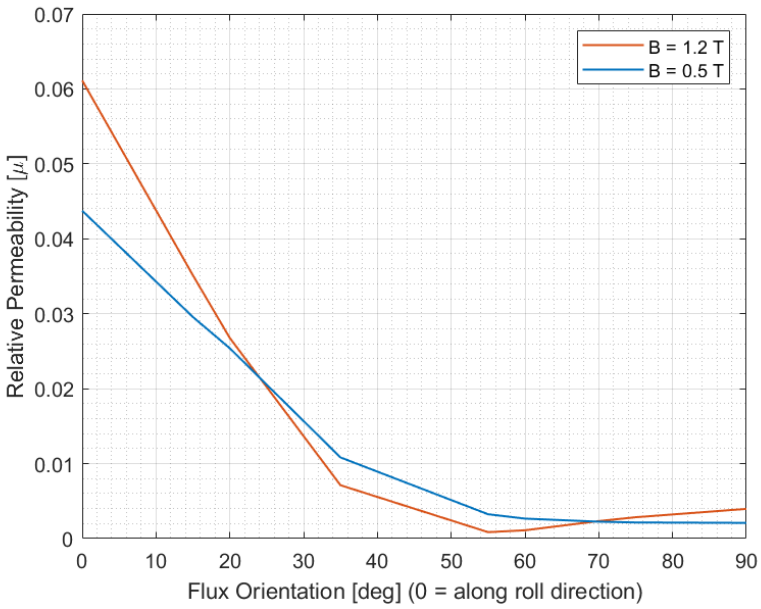


Figure 3.3: The GO steel relative permeability vs flux angle.

Table 3.1: The Mechanical Properties of the Considered Materials

| Material | Yield Stress [MPa] | Density [kg/m$\hat{3}$] |
|---|---|---|
| NO-SiFe | 400 | 7650 |
| GO-SiFe | 320 | 7650 |
| CoFe | 210 | 8120 |
| SMC | 20 | 7500 |

### 3.3.3 Material Properties

The different materials under study have different mechanical and electromagnetic properties. The different mechanical properties of the materials are summarized in Table 3.1. The SMC has significantly worse yield strength than other materials. However, the stator teeth are fully encapsulated with plastic, such that they see very little stress. Similarly, the selected CoFe has been processed in such a way as to maximize electromagnetic properties, at the expense of mechanical strength. In terms of density, the CoFe is about 6 % denser than the other materials.

Electromagnetically, the primary data to compare are the $B-H$ curves of the material, which show the saturation limit and induction of the material, and the core loss curves. Note that for the GO-SiFe material, properties are given at 0° and 90° orientation relative to grain direction. The $B-H$ curves are shown in Fig. 3.4 and the core loss curves at 200 Hz, 600 Hz, 1000 Hz and 1400 Hz are shown in Fig. 3.5. The loss curves shown here are calculated from equation 3.1 and have been fit to supplier test data. Additional loss curves from 50 Hz to at least 2000 Hz are used in the FE model to capture the complete behavior.

The CoFe steel has the best magnetic properties, with good induction, the highest saturation limit, and very low losses. The GO-SiFe has close to the same performance along the grain direction, suffering only from a reduced saturation limit. However, across the grain direction, loss, induction, and the saturation limit are much worse. This is the known drawback of GO steels, and why they are

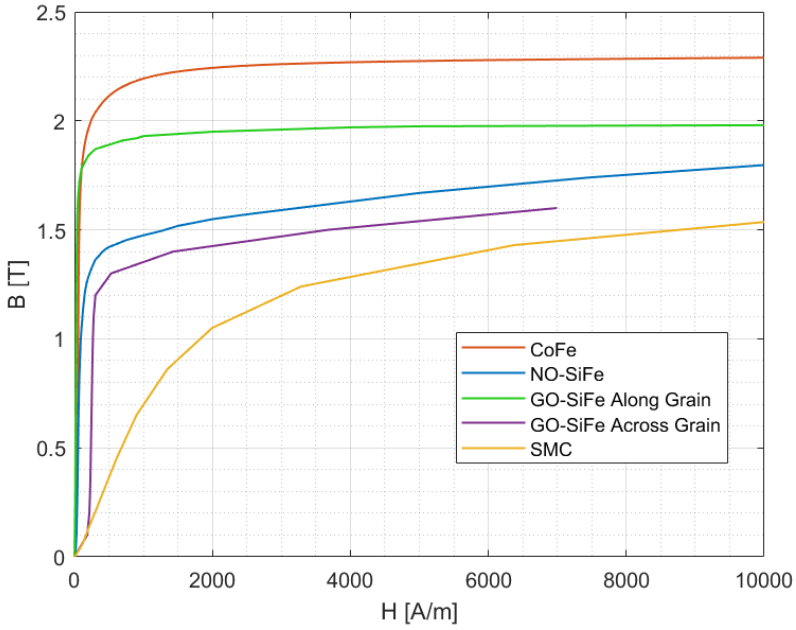


Figure 3.4: A comparison of $B - H$ curves for the materials under study.

only used in machines where the flux orientation is uniform and aligned. The NO-SiFE properties are between the along grain direction and across grain direction properties of the GO-SiFe. Particularly in terms of losses, it is quite competitive, but there is expected to be some consequence in terms of torque production due to the lower saturation limit, with permeability starting to decrease past about 1 T. Finally, the SMC material has reasonably low losses, due to its high resistivity, but also significantly lower permeability. Core loss for all materials is sensitive to frequency and saturation level, where high-speed high-power operation generates the most core loss.

The GO-SiFE core loss across grain direction is poor, and further investigation showed that there is likely uncertainty in these results. As mentioned, the presented loss curves are based on a best fit to supplier test data. For most materials, and along the grain direction of GO-SiFE, the model presented in equation 3.1 fits the test data quite well. This is not the case across the grain direction where the loss model has higher error, exhibiting a different curve shape than the test data.

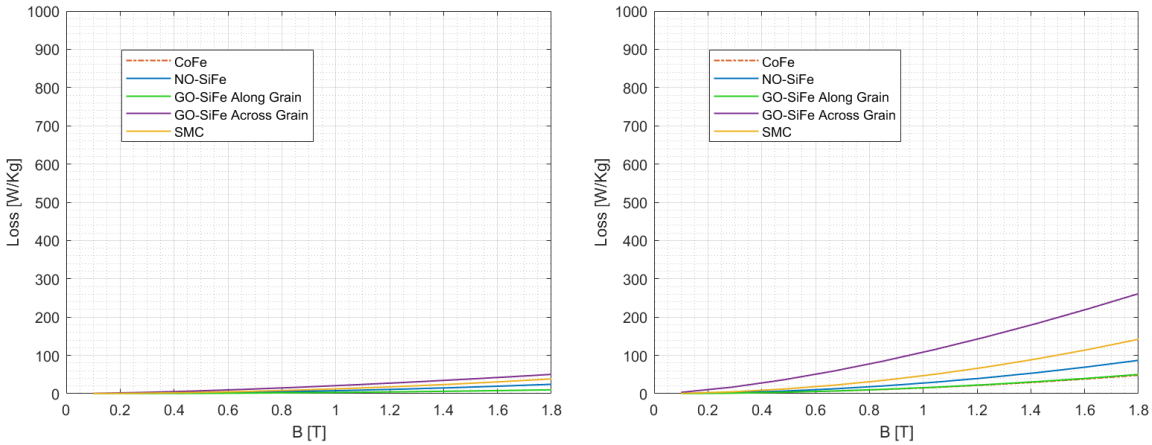


(a)




(b)

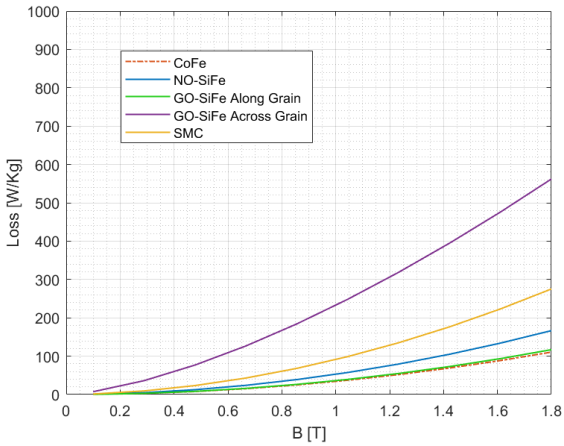


(c)

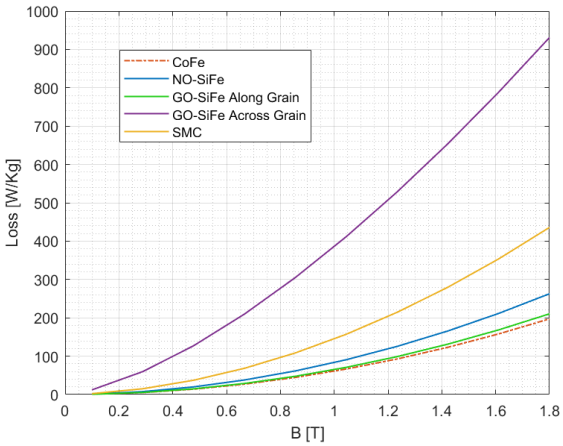


(d)

Figure 3.5: A comparison of core loss density at (a) 200 Hz, (b) 600 Hz, (c) 1000 Hz, and (d) 1400 Hz for the considered materials.

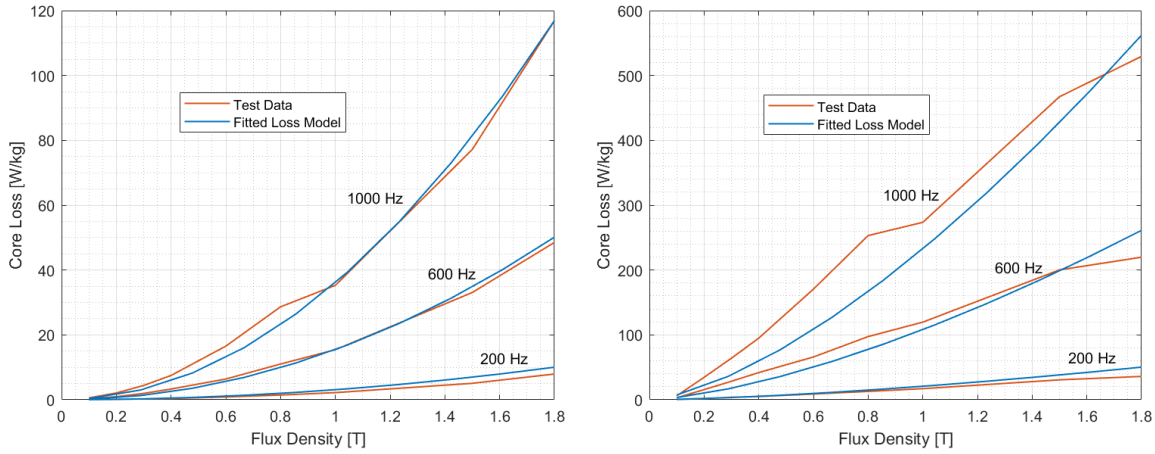


(a) (b)

Figure 3.6: A comparison of the core loss density model versus test data for GO-SiFe (a) along the grain direction, and (b) across the grain direction at three representative frequencies.

This is visible in figure 3.6. This could be due to two primary reasons; the supplier test data has limited data points testing across the grain which introduces error, and/or the proposed loss model does not fit well the GO-SiFe. Unfortunately, further material testing was not possible in the time frame of this research. Hence, the core loss predictions with GO-SiFe steel have some uncertainty which is taken into consideration in the material selection.

### 3.3.4 Manufacturing Considerations

Comparing the different soft magnetic materials, it is also important to analyze manufacturing complexity and cost. As previously discussed, NO-SiFe steels are the most common electric steel in electric machines. Through volume cost savings, and the low cost of raw materials, they are one of the most cost-effective electrical steels. GO-SiFE steel is less common in electric machines, but is widely used in transformers and inductors. It is about 20 % higher cost than NO-SiFe steels [77]. CoFe steels on the other hand, are significantly more expensive due to the high price of cobalt. Ten times higher price than SiFe steels is common [68].

In order to form cores, or in this case individual teeth, laminations must be cut. Strip steel is usually stamped or laser cut to produce individual laminations that are then stacked and bonded to form cores, or in this case, the stator teeth. These processes introduce stresses in the edge of the tooth which can worsen the magnetic properties of the material [78]. These stresses can be relieved by annealing, which improves the magnetic properties [79]. This effect is significantly larger with CoFe steels as compared to SiFe steels [68], [79]. Cores made with CoFe laminations must be properly annealed to maintain their magnetic properties, adding another cost factor to this material.

Alternatively, the tooth can be stacked as a rectangular block, and the final shape cut using wire electrical discharge machining (EDM). Wire EDM has been shown to have less effect than stamping on the magnetic properties of the material, so annealing is less necessary [80]. As well, with wire EDM, it is possible to form the smooth sided trapezoidal shape desired for the tooth. Otherwise, with a stamping process, there would need to be steps in the trapezoid shape, as shown in Fig. 3.7. Wire EDM is a much slower process than stamping and stacking laminations, so has limited applicability outside of prototype or low volume production. In the initial prototyping stages of this project, the cores will be EDM cut. Hence, the trapezoidal tooth design is chosen. In later work, if the prototype volume increases, the core may be stamped and stacked, however in either case the tooth cross sectional area will be maintained.

### 3.3.5 Lamination Orientation

The lamination direction in the tooth is important with electrical steel. Referring to Fig. 3.2, we see that the flux vectors are primarily axial, and to some degree circumferential. There is no significant component of the flux that travels radially. Hence it is presumed that the best direction of lamination is stacked along the radial direction (Fig. 3.8a). This was verified by simulating the model with NO-SiFE steel, but with circumferentially stacked laminations (Fig. 3.8b). Torque reduced by 1.2 % and core loss increased by over 450 %. This is because of rotor flux passing though unexcited teeth of the stator. This flux is not generated torque and can be referred to as rotor leakage flux. In Fig. 3.9, the flux vector field is plotted in the same two teeth at the same time step, where in the first simulation the teeth are radially laminated (a), and in (b) the teeth are circumferentially laminated. The leakage flux path is highlighted with the red arrow. The increased magnetic reluctance in the circumferential direction (b) due to the small air gaps between laminations, causes the leakage flux to pass from one rotor to the next, through the tooth, exciting much more of the tooth and forming a large loop. In the reference machine with radial lamination, the low magnetic reluctance in the circumferential direction allows the leakage flux to form a small loop from one magnet pole to the next without exciting the entire tooth. This simulation verifies the initial hypothesis, and all steels will be radially laminated.

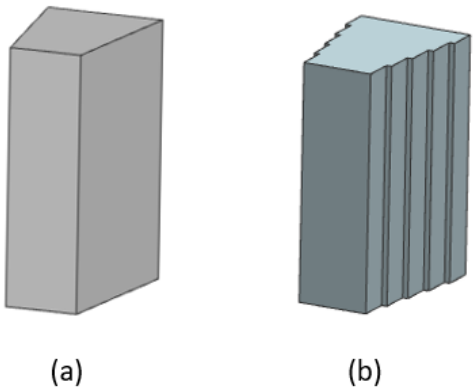


Figure 3.7: A comparison between an EDM cut core (a) and a stacked core (b).

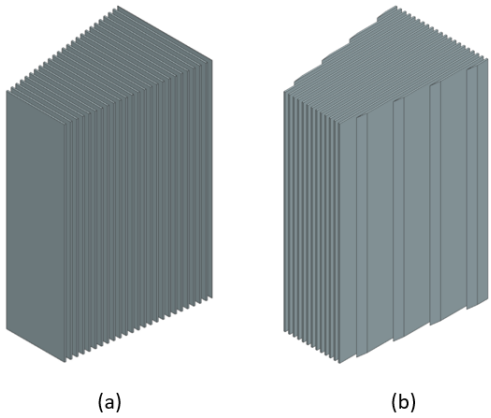


Figure 3.8: The radially laminated (a) and circumferentially laminated (b) tooth.

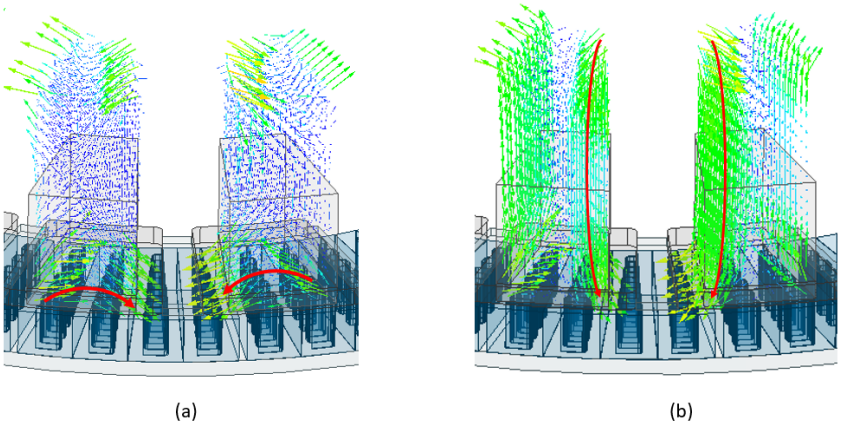


Figure 3.9: A comparison of leakage flux paths through unexcited stator teeth for radially laminated (a) and circumferentially laminated (b) steel.

Table 3.2: A Comparison of Performance with the Considered Tooth Materials at the Continuous Power Operating Point

| Tooth Material | NO-SiFe | GO-SiFe | CoFe | SMC |
|---|---|---|---|---|
| Torque [p.u.] | 1 | 1.028 | 1.061 | 0.971 |
| Core Loss [p.u.] | 1 | 1.318 | 0.858 | 1.143 |

### 3.3.6 Results

The baseline model with NO-SiFe is studied at the maximum continuous power condition of about 100 kW, and the peak power condition 20% higher, and is compared to the other three considered materials. The results are presented in tables 3.2 and 3.3. Values are normalized to a reference here and throughout the thesis to protect project confidentiality. At the continuous power point, as expected, CoFe steel provides the best torque and lowest losses, with a 6 % improvement over the NO-SiFe in torque, and 14 % lower losses. The GO-SiFe is in between, with relatively good torque, 3 % higher than the baseline, but lower than the CoFe. However, the core loss is noticeably worse, 32 % higher than the baseline, and much higher than CoFe. This is due to the particularly poor GO-SiFe loss across the grain direction. The area with the least oriented flux is the tooth tip, and this is also an area of high flux density, which noticeably compromises the GO steel. Finally, the SMC has significantly lower performance, with also somewhat elevated losses. It is only used in the pole shoe for its ease of manufacturing, and the three-dimensional flux paths in this region. In the peak power condition the trends are very similar, though the core loss is relatively insensitive to the power level.

Based on this data alone, it would seem clear that the CoFe steel is the clear choice. However, as identified while discussing manufacturing constraints of these different materials, the cost and manufacturing complexity are very high. With only a 6 % torque improvement over GO steel, the significant cost increase was not

feasible for this project. As well, the CoFe teeth are 6 % heavier than SiFe steel. Hence, the GO steel is a very attractive choice. However, core loss is a concern as compared to NO-SiFe. If the excitation current of the machine with NO-SiFe teeth is increased to match the torque output of the Go-SiFe steel, the loss results are more even. This is shown in table 3.4 where all the components of loss are shown. Since copper loss and rotor loss are also dependent on the excitation current, they must be considered in the comparison. Taking into account all contributions, and comparing between NO-SiFe and GO-SiFe, there is a 3.8 % increase in loss with GO steel at continuous power, and 1.1 % increase at peak power. In terms of copper loss, there is a 4 % improvement using GO steel, while rotor losses stay constant.

Ultimately, the GO-SiFe was chosen, and for the following reasons. Most importantly, thermal models of this machine identified the winding as a primary area of concern in terms of hot spots, and potential insulation damage. As such, reducing copper loss and subsequent high winding temperature is important. An effective way to do this is by reducing the excitation current by increasing torque/ampere of the machine. GO-SiFe has the best torque/ampere of any material other than CoFe. Second, as mentioned previously, the across grain direction GO steel loss data is derived from a limited data set, so some uncertainty in core loss prediction is expected. The small, 1-3 % difference in loss as compared to NO-SiFe is considered negligible compared to the known benefit of the copper loss reduction. Unfortunately, further material testing was not possible within the constraints of this project.

Table 3.3: A Comparison of Performance with the Considered Tooth Materials at the Peak Power Operating Point

| Tooth Material | NO-SiFe | GO-SiFe | CoFe | SMC |
|---|---|---|---|---|
| Torque [p.u.] | 1.191 | 1.224 | 1.270 | 1.162 |
| Core Loss [p.u.] | 1.026 | 1.347 | 0.882 | 1.121 |

Table 3.4: A Comparison of GO and NO Steel at Continuous and Peak Power with Adjusted Excitation Current

| Tooth Material | NO-SiFe | GO-SiFe | NO-SiFe (peak) | GO-SiFe (peak) |
|---|---|---|---|---|
| Torque [p.u.] | 1 | 1 | 1.188 | 1.189 |
| Stator Core Loss [p.u.] | 1 | 1.311 | 1.038 | 1.340 |
| Copper Loss[p.u.] | 1 | 0.968 | 1.510 | 1.453 |
| Total Loss [p.u.] | 1 | 1.038 | 1.389 | 1.406 |

## 3.4 Chapter Summary

Magnetic material selection is a primary consideration in any machine design. It affects performance, weight, cost, and manufacturing. In aerospace applications, high performance, particularly power density, is critically important. The selection of soft magnetic materials was reviewed for electric machines in aerospace applications. In a YASA AFPMSM, the unique stator tooth design and uniform magnetic flux path provide opportunity for less commonly used magnetic materials, like GO-SiFe and SMC. The review also showed that CoFe steel is often used for high performance aerospace applications. NO-SiFe was identified as the baseline material, widely used in many electric machine applications. Four materials of interest were selected and introduced for study: Vacodur 49 210 MPa CoFe steel, NO20 NO-SiFe Steel, M80-23P GO-SiFe Steel, and Somaloy 700HR 5P 800MPa SMC. Modeling of these materials in FE software was discussed, with particular attention on the modeling of GO-SiFe with its anisotropic material properties.

The study comparing these materials was then undertaken. The material properties were analyzed and compared. Manufacturing considerations were discussed, noting that CoFe has additional requirements for manufacturing, as well as high raw material cost. Then the lamination stacking orientation was analyzed, and it was validated that if using laminated electrical steels, there is a clear preference for radial stacking. Finally, the four soft magnetic materials were compared for performance and losses through three-dimensional FE simulation. It was found that CoFe has the best performance with the lowest losses. However, material cost and manufacturing complexity where ultimately prohibitive for this project. GO-SiFe and NO-SiFe were similar in performance, with GO-SiFe having better torque per ampere but worse core losses. SMC material was used for the pole shoes in all cases, but when used for the entire tooth, torque dropped considerably, and losses rose. To make a final material decision, further analysis of the machine with GO-SiFe and NO-SiFe was carried out. Losses for the entire machine were compared, and it was shown that while the machine with GO-SiFe steel had slightly higher losses in some operating conditions, the higher torque per ampere resulted in about 4 % lower copper losses for the primary operating condition. Thermal analysis of the machine showed that reducing copper loss was a priority in order to reduce the highest temperature in the machine. Hence, GO-SiFe is chosen as the material for the stator teeth, with SMC pole shoes. The next chapter expands on the stator design by studying how to further reduce copper loss.

# Chapter 4

# Analysis and Reduction of AC Copper Loss

## 4.1 Introduction

In the previous chapters, the baseline machine was introduced, and the stator magnetic materials were studied. Working from this design, the next study is to improve the efficiency of the machine by further reducing copper loss. This is undertaken by modifying the stator, winding, and wire geometry. As previously introduced, the machine is a single-stator double-rotor YASA AFPMSM, with 18 slots and 16 poles. The winding is a double layer, concentrated winding. This design has a high winding factor, and the high pole count increases the machine torque density. To further increase the power density, large cross-sectional area (CSA) rectangular conductors are employed in the stator winding [81], [82]. As stated previously, copper loss is the largest loss contributor in the proposed machine with an approximately 30 % contribution from the AC copper losses. This study aims to reduce the total copper loss with focus on reducing the AC loss contribution.

AC copper losses originate from skin effect, proximity effect, and induced eddy currents from rotor leakage fluxes [83]. These origins are investigated here, and the affecting parameters are identified, considering different operating conditions such as temperature and frequency which affect the winding resistance [83]. As well, modeling of AC losses is discussed. The chosen modeling method follows closely with the previously introduced approach to modeling an AFPMSM, but further details are presented on the modeling individual conductors to accurately capture the AC copper loss.

After identifying the origins of AC loss, multiple geometry modifications are proposed and their effectiveness at reducing total copper loss is assessed. The total copper loss, as well as the AC/DC loss ratio, are used as a metric for the relative contribution of AC losses. The loss ratio is defined as the total copper loss divided by the DC copper loss (eqn. 4.1). Finally, a set of guidelines is proposed for reducing AC loss, and a final machine design is presented.

$$\frac{AC}{DC} = \frac{Loss_{Total}}{Loss_{DC}} \tag{4.1}$$

## 4.2 Review of AC Copper Losses

### 4.2.1 Origins of AC Copper Loss

AC currents traveling in a conductor have an uneven distribution, with a higher concentration of current close to the conductor surface, which is known as the skin effect. The strength of the skin effect is defined by the skin depth, which is the distance from the outer surface to the point at which the current density has reduced exponentially $1/e$ times, where $e$ is 2.71828 [83]. The skin depth is obtained from eqn. 4.2 where $\rho$ and $\mu_r$ are the resistivity and the permeability of the conductor, respectively. $f$ is the frequency of the excitation current and $\mu_o$ is the permeability of free space [83], [84].

$$\delta = \sqrt{\frac{\rho}{\pi f \mu_o \mu_r}} \tag{4.2}$$

The skin effect effectively reduces the CSA of the conductor, by limiting the area in which current flows. This increases the effective conductor resistance and generates more losses. It is evident from eqn. 4.2 that skin depth decreases as frequency increases, and, hence, resistance increases. The phenomenon is caused according to Faraday's law [84]. When an AC current passes through a conductor, it generates a magnetic field perpendicular to the conductor. This field induces an eddy current with flows along with the primary current direction at the surface of the conductor, and against the primary current at the center [84].

The AFPMSM studied here operates in a range of 0-1 kHz fundamental excitation frequency. This corresponds to a minimum skin depth of 2.25 mm, which is more than 50 % of the considered conductor largest dimension. Hence, although there is a current concentration at the outer surface of the conductor, the skin effect is low. To visualize the skin effect, a representative conductor cross section

is excited at 100 Hz and 1 kHz fundamental frequency, as shown in Fig. 1a and 1b. At 1 kHz, the current is concentrated at the conductor surface, illustrating the skin effect, whereas the current density is uniform at 100 Hz since the skin depth is much larger than the conductor dimensions. The skin depth is also dependent on conductor resistance, as can be seen in eqn. 4.1, and the conductor resistance increases with temperature [83]. Fig. 4.1c. shows the reduction in current concentration due to skin effect when the conductor is at 100 C.

Skin effect is only a complete description of AC loss for individual conductors in air, such as in the end winding connections of the machine. For conductors placed close together in a slot, AC losses are generated through what is called proximity effect, which creates a current concentration in the conductor [49], [83]. This effect is first discussed in the case of two conductors in proximity in air. When two wires are placed in proximity, the magnetic field around each wire excites an eddy current along the length of the proximate wire. With an in-phase excitation this eddy current travels along the direction of primary current on the furthest apart surfaces of the wire, increasing current density in that region. The return loop of the eddy current on the close surfaces of the wire, opposes the direction of primary current, thereby reducing current density in that region. The magnitude of the proximity effect is dependent on the excitation frequency in addition to current phase and magnitude, temperature, and distance between conductors.

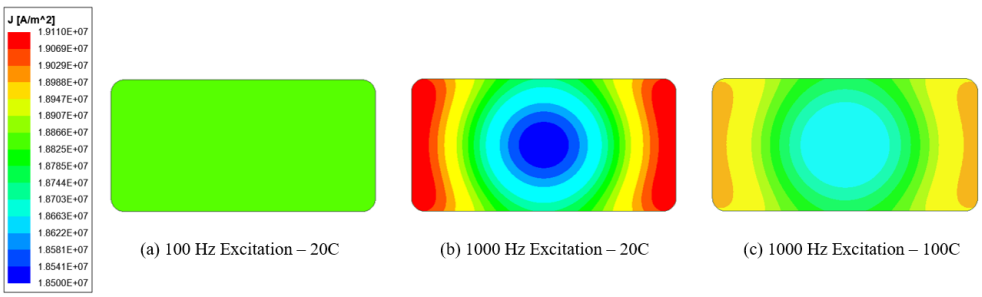


Figure 4.1: The impact of skin effect on current density for a representative conductor.

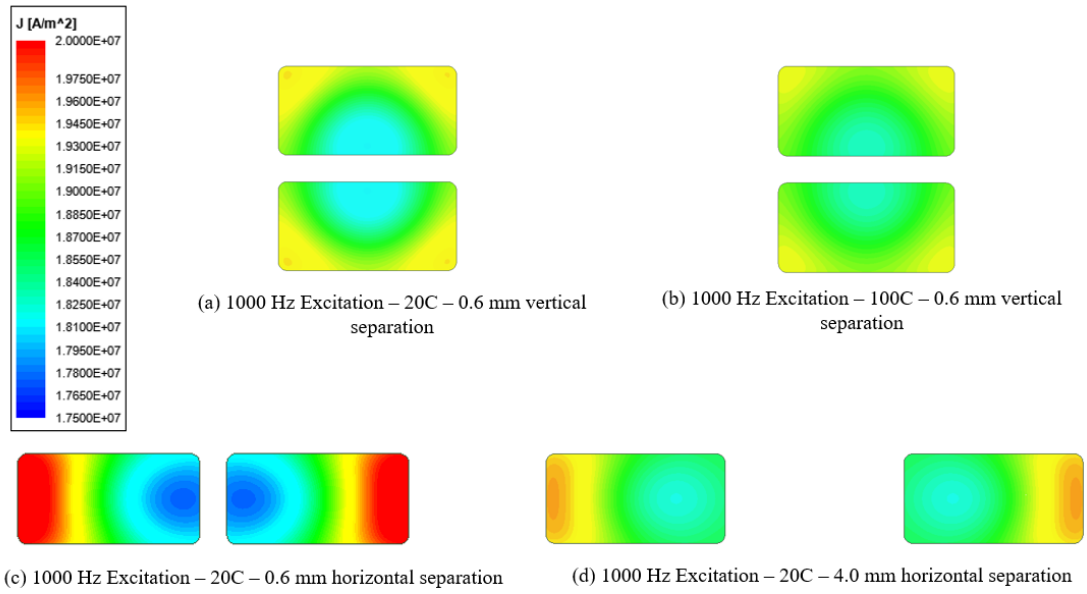


Figure 4.2: The impact of proximity effect on current density for vertically (a), (b), and horizontally (c), (d) spaced conductors at 20 C (a), (b), (c) and 100 C (b) with 150 Arms 1000 Hz in-phase current excitation.

Figs. 4.2a and b show a 1 kHz fundamental excitation of two conductors vertically separated, as they would be in two turns of the coil, at 20 C and 100 C. In this case the two excitations are in phase, and the current density distribution is symmetric and concentrated in the corners. Similar to the skin effect, the proximity effect is reduced at elevated temperature due to the increased conductor resistance, which reduces the magnitude of the circulating eddy currents. Fig. 4.2c shows two conductors with the same separation distance, current excitation, and temperature as Fig. 4.2a but spaced horizontally. The peak current concentration is about 2.5 % larger in this configuration, due to the smaller dimensions of the wire being closest, thereby concentrating the eddy currents along a smaller surface. As well, though the current concentration increases in a radial fashion relative to the center of the close surfaces of the wire, the larger width of the wire makes this current concentration appear along the sides, as opposed to in the corner in Figs. 4.2a and b. Finally, Fig. 4.2d compares two conductors with the same excitation as Fig. 4.2c, but with much larger spacing between them. As can be

seen, the proximity effect reduces with distance, as the effect from the magnetic fields around each wire is reduced.

Fig. 4.3a shows two conductors horizontally separated with a 1 kHz fundamental excitation, but 120° out of phase. In the concentrated type double layer winding, some slots contain two coils belonging to different phases. As can be seen in the figure, this has an impact on the proximity effect, where an in-phase excitation creates a symmetric current distribution, and the out of phase distribution is uneven due to the unbalanced magnetic fields generated by the two conductors. Fig. 4.3b shows the same wire configuration and excitation, but at reduced current, demonstrating the dependence of proximity effect on current magnitude.

While it is convenient to illustrate the sensitivities of proximity effect by studying the behavior of conductors in air, this is not the real case in a machine. For conductors in a slot of a stator, the magnetic fields created by the excited conductors are impacted by the highly permeable iron core. Instead of a magnetic field around just the conductors, a magnetic field passes through the teeth, and from one tooth to the next. Inside the slot, this magnetic field tends to flow horizontally, from one tooth to the next, when the coils in the slot are in phase, and vertically, when the coils are out of phase. This can be seen in Fig. 4.4, and Fig. 4.5, for the case of in and out of phase, respectively. Note that the magnitude of current concentration is also much greater than the isolated cases of conductors proximate in air. As well, for in phase excitation, the flux field from proximity effect is strongest near the airgap, causing the highest loss in the conductors close to the airgap. The exact magnetic field flow is highly dependent on the tooth shape, if there is shaping at the tooth tip, and the conductor placement within the slot. The previously identified dependencies on frequency, temperature and current also hold.

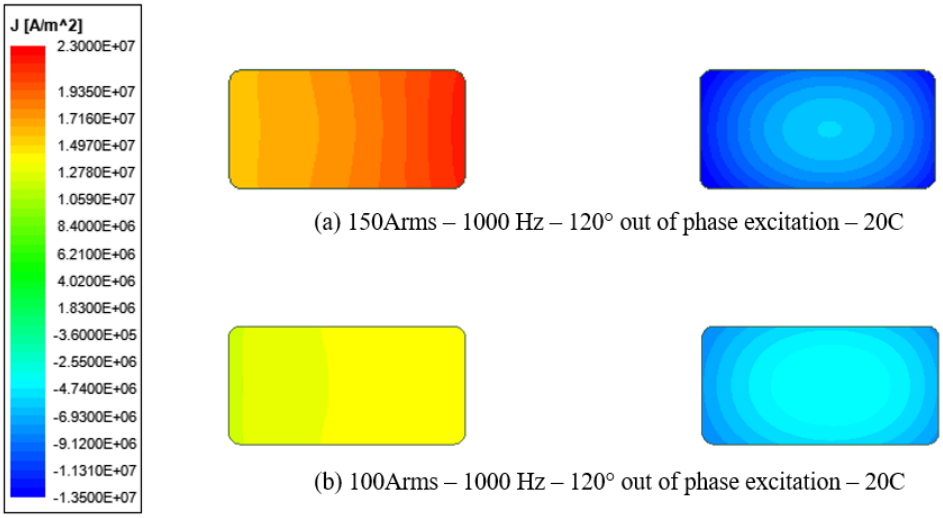


Figure 4.3: The impact of proximity effect on current density for horizontally spaced conductors with 1000 Hz out of phase excitation at 150 Arms (a) and 100 Arms (b) at 20 C.

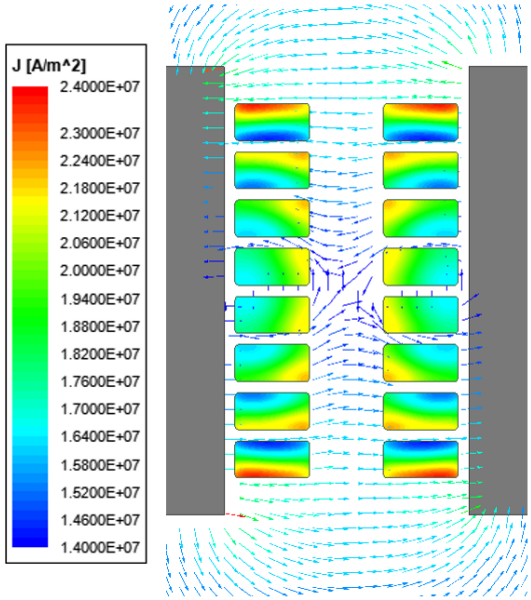


Figure 4.4: The impact of proximity effect on current density for conductors in a slot, with 1000 Hz in phase excitation at 150 Arms

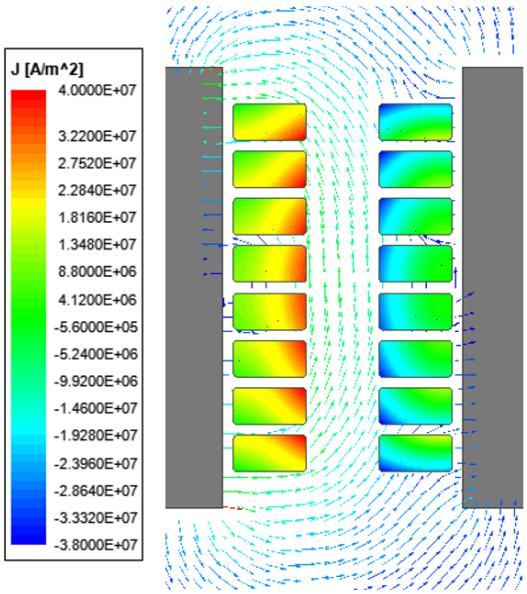


Figure 4.5: The impact of proximity effect on current density for conductors in a slot, with 1000 Hz out of phase excitation at 150 Arms

As well as proximity effect, leakage flux is a significant contributor to AC loss [49], [55], [56], [83]. Here leakage flux refers to rotor generated leakage flux, that is, flux generated by the rotor that impacts the field distribution around the slot and conductors, thereby generating AC loss. This is generally strongest in the conductors closest to the airgap since they are close to the rotor, and is also more commonly seen with relatively large slot openings [49]. This flux path is often a consequence of the primary, torque generating flux path, but which unintentionally impacts the winding if the path is not well controlled and interacts with conductors. For an AFPMSM, these leakage flux paths are three-dimensional [55], and various machine features such as pole shoes and wedges should be carefully designed to limit leakage fluxes and control flux paths.

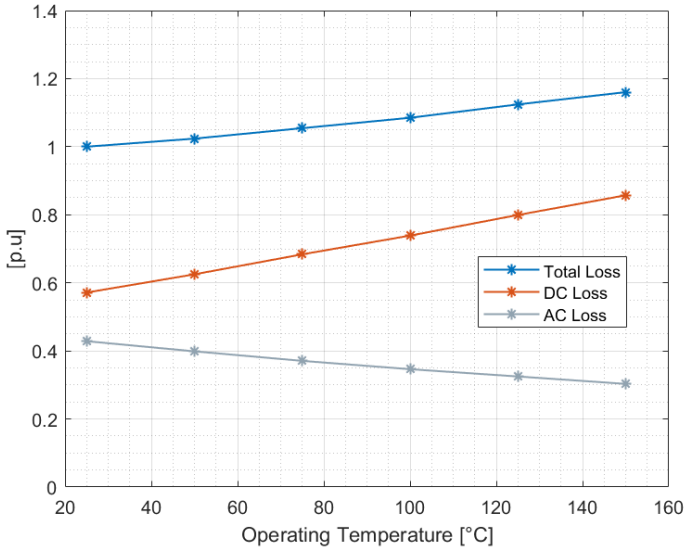


Figure 4.6: The impact of operating temperature on copper loss.

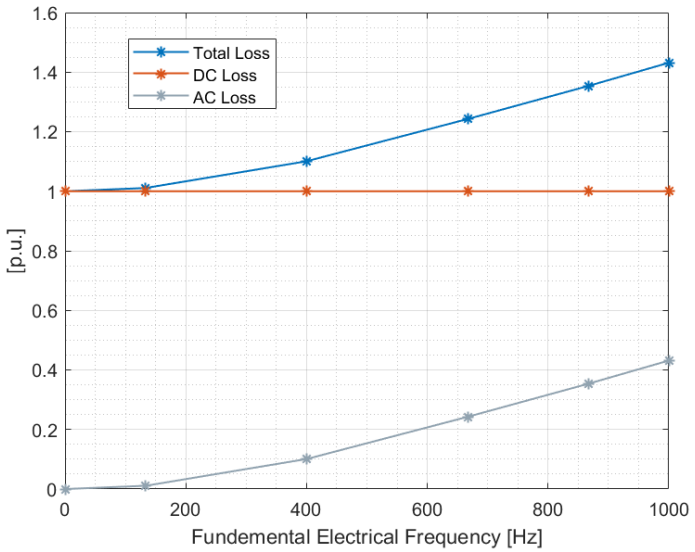


Figure 4.7: The impact of operating frequency on copper loss.

As previously discussed in the context of skin or proximity effect, the winding resistance increases with temperature. As resistivity increases, the magnitude of eddy currents is reduced, which reduces AC loss [83]. It is harder to isolate this impact for leakage flux effects since they are dependent on the machine geometry. However, the overall effect of temperature on copper loss for the considered machine can be seen in Fig. 4.6, considering all AC loss origins. In terms of frequency, as was previously identified in Fig. 4.1, the current concentration effect due to leakage flux is highly frequency dependent. The effect of frequency on copper losses is shown in Fig. 4.7 for the considered machine. The relationship between copper loss and operating condition is important to understand for axial flux machines with large cross section conductors, as AC losses can be a significant contribution.

## 4.3 Study of AC Copper Loss

All models under study are derived from the baseline model and simulated using a three-dimensional FE simulation as introduced in Chapter 2. The model is simulated in ANSYS Maxwell, as a three-dimensional time transient simulation. The model takes advantage of the quarter symmetry of the machine, as shown in Fig. 4.8, to reduce the simulation time. The individual coil conductors are modeled, which is necessary to capture the AC copper loss effects. The mesh of the coil model is critical to be able to capture eddy currents in the copper. The max mesh element size in the conductor is chosen such that the average element length is about 50 % of the skin depth. This ensures creating, on average, two mesh layers in the skin depth of the conductor. While the FE model has individual conductors modeled, it does not account for the end winding connections of the machine. However, AC losses in the end winding are negligible due to the relatively large spacing between conductors, the long distance away from rotor leakage flux paths, and the negligible skin effects. As such, a hybrid model is utilized, where the DC losses are calculated analytically according to eqn. 4.3, based on the real total wire length $l_w$, CSA, wire resistance $\rho$, which is dependent on temperature, and the excitation current $I$ in Ampere root mean square (Arms).

$$Loss_{DC} = I^2 * [\frac{l_w}{CSA} * \rho] \tag{4.3}$$

The machine is simulated at its nominal operating condition, with an assumed winding temperature of 150 °C. The excitation current is adjusted to maintain the output torque within 1 Nm of nominal, as some machine modifications change the generated torque/ampere. In all simulation cases, the total copper loss and AC/DC loss ratio are captured. The original design is simulated at continuous-power condition, primary operating speed, and a nominal winding temperature of 150 °C. A baseline of total copper loss is established at approximately 2.5 kW,

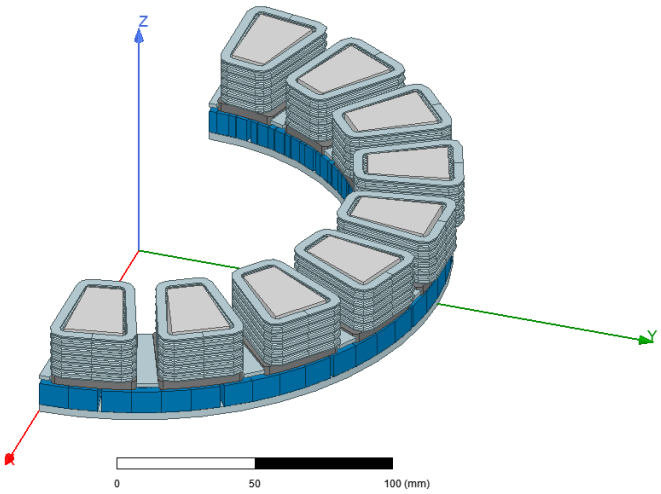


Figure 4.8: The FE model of the reference machine.

with an AC/DC loss ratio of 1.354. The current density distribution is plotted for the full winding in Fig. 4.9. It is immediately observed that there is a high current concentration on the coil turns closest to the slot opening, approaching 160 A/mm$^2$, considerably over the DC peak current density of 26 A/mm$^2$. In Fig. 4.10, a cross-section of this area of concern is investigated more closely, plotting the flux paths and flux density as well. There is a strong flux path right next to the conductor closest to the airgap which induces significant eddy currents in this conductor, particularly in the corner circled in red. This flux path is a combination of the proximity effect and the rotor leakage flux. As well, there is the proximity effect between teeth (the weaker flux lines passing from the left to right in the slot) which is causing additional, though weaker current concentrations in other conductors in the slot. The following studies focus on addressing these issues. Proposed studies investigate the conductor geometry by modifying conductor CSA, aspect ratio, and placement in the slot. As well, the stator geometry is studied by modifying the tooth length and pole shoe design.

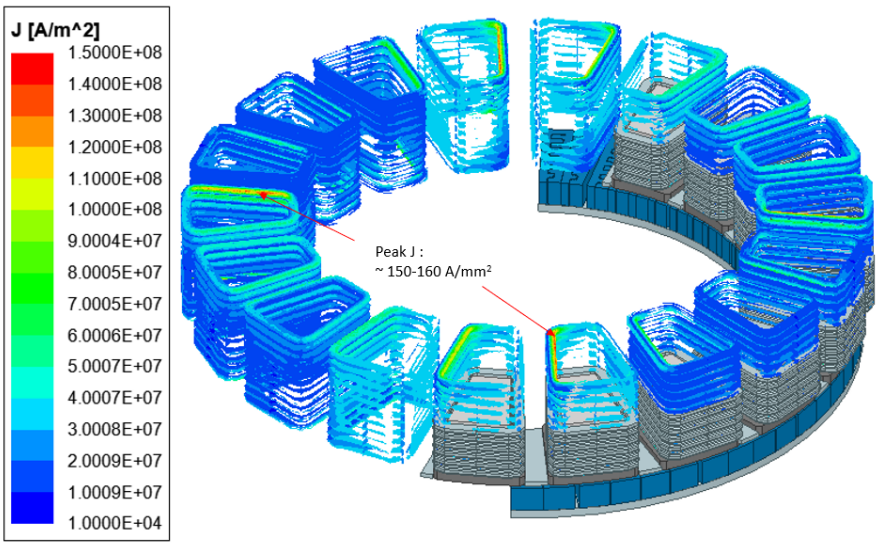


Figure 4.9: The current density in the winding of the reference machine.

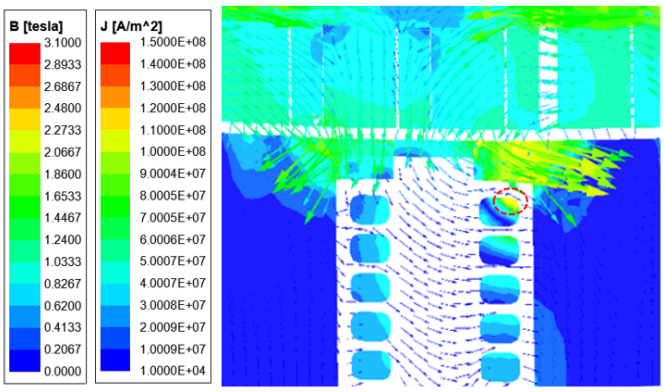


Figure 4.10: The flux field and current density in the area of concern for the reference machine.

### 4.3.1 Effect of Conductor Cross Section

The conductor geometry, stator tooth length, and wire position in the slot, are the first area of investigation in reducing AC copper loss. Modifying the wire CSA is a way to balance AC versus DC copper loss, as well as the copper weight. The conductor CSA is varied here by 10 % smaller area than baseline, and then 10 % and 20 % larger, while maintained the conductor thickness. As such, the conductor aspect ratio is also modified, by 10 % smaller, 10 % larger, and 19 % larger. According to Fig. 4.11, we can see that total copper loss is mostly constant across a range of wire sizes, with a minor increase in losses as the conductor area gets smaller. At the same frequency and temperature, as the conductor area increases, the decrease in DC loss is almost canceled by the AC loss increase.

When the conductor area modification is studied at higher or lower frequency operation, a clearer picture emerges of the balance between AC and DC loss and how it is affected by conductor CSA. In Fig. 4.12 the total copper loss is plotted across the range of fundamental operating frequencies of the machine for the variation of CSA under study. The total copper loss at each frequency is normalized to the copper loss with the baseline wire at that frequency. This plot shows how at lower operating frequencies, total loss decreases with increasing CSA, due to the dominance of DC copper loss. Then, at some point, the copper loss becomes relatively insensitive to changes in the CSA. This occurs around the nominal operating frequency for this machine, as seen in Fig. 4.11. However, if the excitation frequency were to be further increased, we would expect to see reduced losses with reduced conductor CSA, due to the increased dominance of AC loss.

A similar study is done with respect to changing operating temperature. In Fig. 4.13 the total copper loss is plotted for temperatures ranging from 25 C to 150 C, but with the operated frequency fixed at the nominal (867 Hz) frequency. Similar to before, the total copper loss at each temperature is normalized to the copper loss with the baseline wire at that temperature. As temperature decreases,

copper loss increases with increasing wire size due to reduction in resistance, which increases the dominance of AC loss. Whereas at higher temperatures, copper loss is less sensitive to wire size because AC and DC copper loss are more balanced. Note again that in both of these studies, the total magnitude of loss is not considered, just the normalized loss relative to the loss with the baseline wire size. In both cases of either lower frequency or lower temperature operation, the total copper loss decreases when just looking at magnitude. This study illustrates what is the best wire size at given operating condition.

For many machines, there may be an operating region where the total copper loss is relatively insensitive to the conductor CSA. If this is the primary operating condition as here, it makes sense to minimize the wire size to reduce weight. Otherwise, the conductor size should be defined to minimize total losses considering weight, cost, and manufacturability.

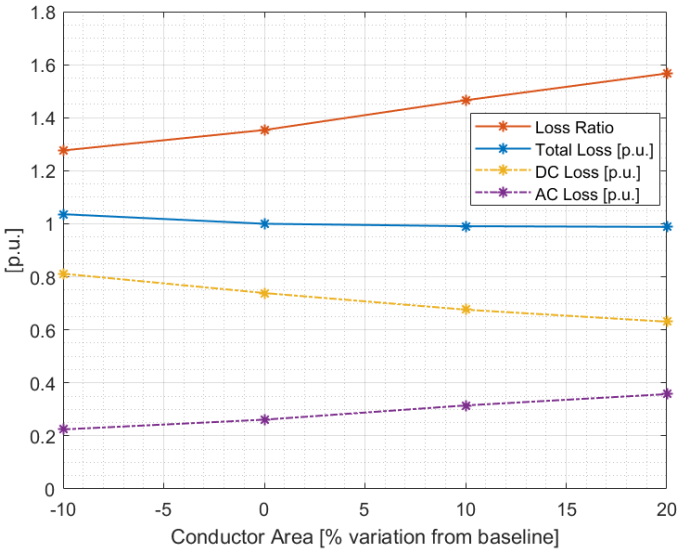


Figure 4.11: The impact of conductor CSA on copper loss.

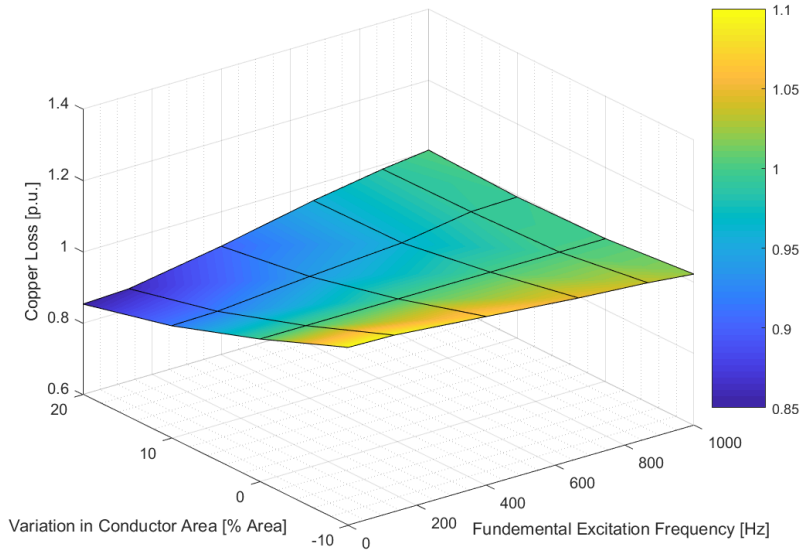


Figure 4.12: The impact of conductor area and operating frequency on normalized copper loss.

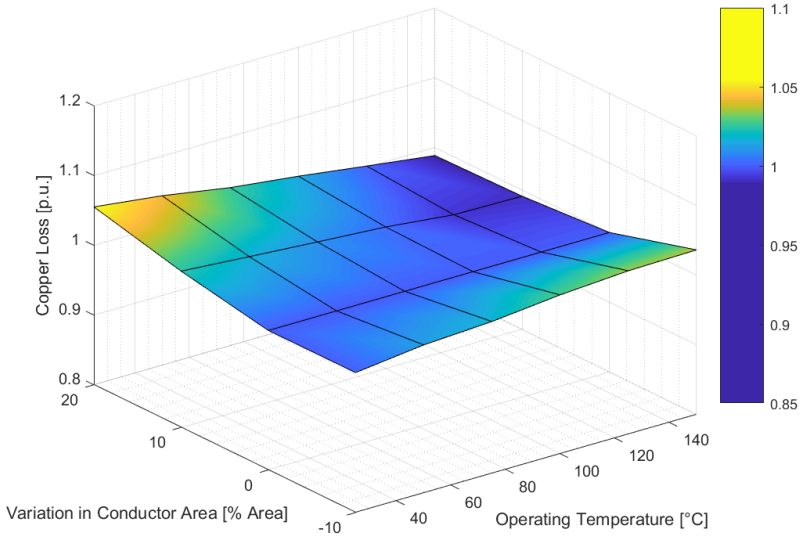


Figure 4.13: The impact of conductor area and operating temperature on normalized copper loss.

### 4.3.2 Effect of Conductor Aspect Ratio

Instead of changing the conductor CSA, just the aspect ratio of the conductor can be modified. The aspect ratio is the ratio of the conductor width to thickness, as identified in Fig. 4.14. As the aspect ratio increases, for a constant CSA, the conductor becomes thinner in the axial direction. This reduces the overall height of the coil, moving the conductors away from the airgap, and the area of high rotor leakage flux and proximity effect (Fig. 4.14). With the higher aspect ratio and wider conductor, the wire length does increase slightly due to the larger path of the wire required to wrap around the stator tooth. Modifying the conductor aspect ratio should reduce total loss, but with less consequence in copper weight as compared to modifying CSA.

The conductor aspect ratio is modified by increasing the width by 10 %, 20 %, and 30 %, and then reducing the conductor height accordingly to maintain the same CSA, leading respectively to a 21 %, 45 %, and 69 % increase in the aspect ratio (Fig. 4.14). The total copper length and weight increase by about 0.8 % for each increase in the aspect ratio, due to the increased diameter path the wire follows around each tooth. The axial spacing between conductors is maintained, but the total height of the coil is reduced, which increases space between the coil and the airgap. For the 10 %, 20 %, and 30 % wider wire, the closest conductor to the airgap is moved 1.3 mm, 2.4 mm, and 3.3mm further away from the airgap, respectively. In the results presented in Fig. 4.15, we see a significant reduction in total losses, with almost a 10 % reduction in copper loss with the highest aspect ratio wire, which is now 8.25 mm away from the airgap. Further investigation of the current density plot for the largest aspect ratio wire (Fig. 4.16) shows that the current density is reduced in the conductor of concern as compared to Fig. 4.10. Moreover, the proximity effect between teeth is reduced by reducing the height of the conductor. The predominant flux path moves tangentially between teeth (left to right horizontally in this view) which excites an eddy current that circulates

into and out of the page as discussed in section 4.2.1. Limiting the conductor height reduces the eddy current path area and magnitude, reducing losses.

Further increase in the aspect ratio and subsequent reduction in the coil height was not possible here due to limitations in the ability to bend the high aspect ratio wire in the end winding connections. The coil windings shown in Fig. 4.17, with very high-aspect-ratio conductors may be a good choice for this type of machine if feasible.

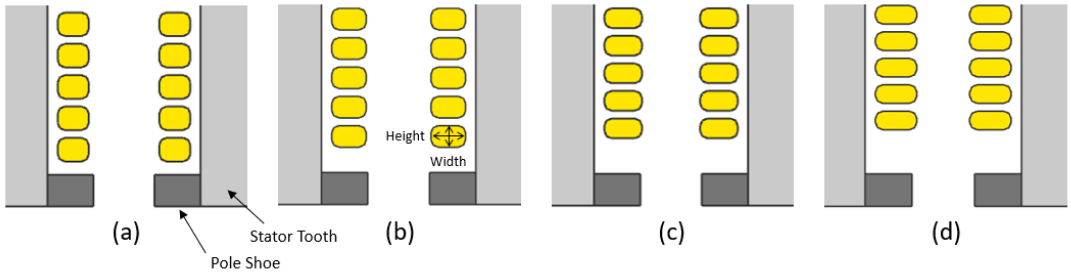


Figure 4.14: The variation of wire aspect ratio: (a) baseline aspect ratio, (b) 21 % larger, (c) 45 % larger, (d) 69 % larger.

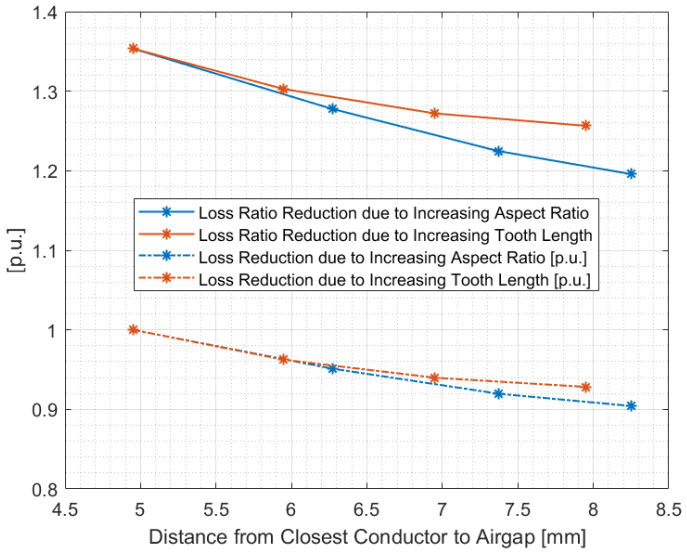


Figure 4.15: The impact of increasing aspect ratio and increasing axial length on copper loss.

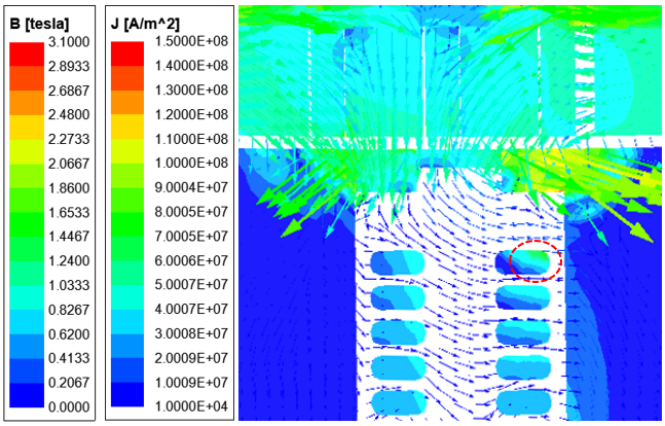


Figure 4.16: The flux field and current density in the area of concern for the 69% increase in aspect ratio conductor.

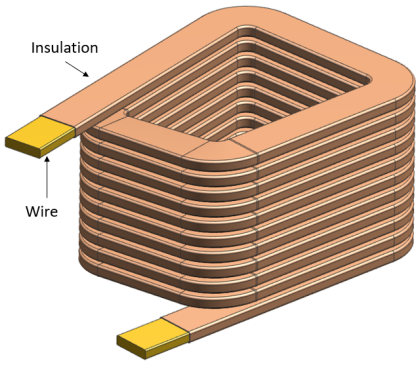


Figure 4.17: An example of high aspect ratio wire.

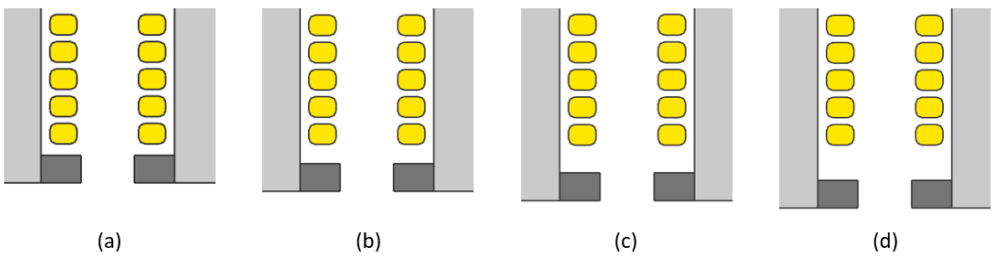


Figure 4.18: The variation in stator tooth axial length: (a) base design, (b) 2mm longer, (c) 4mm longer, (d) 6mm longer.

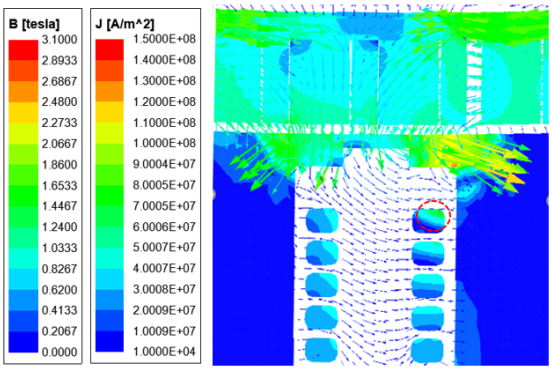


Figure 4.19: The flux field and current density in the area of concern for the 6mm longer tooth.

### 4.3.3 Effect of Stator Tooth Length

In the base design, the stator tooth length is set such that there is enough space for the coil, but not longer, which would increase the weight and volume of the machine. However, making the tooth longer, and having the coil further away from the airgap, as shown in Fig. 4.18, can be beneficial in reducing the rotor leakage flux passing through the conductor closest to the airgap.

The tooth axial length is extended by 2 mm, 4 mm, and 6 mm (Fig. 4.18). As can be seen in Fig. 4.15, increasing the tooth length reduces the total loss by about 4 %, 6 % and 7.5 % as the distance from the nearest conductor to the airgap increases. Studying in detail the 6mm longer tooth, the negative impact of the flux path close to the airgap is reduced (Fig. 4.19). Core loss does increase, by about 2-3 % per 2mm increase in axial length. However, the baseline of core loss is considerably lower than the total copper loss, leading to an overall improvement in machine efficiency by increasing the stator tooth length. The primary tradeoff is an increase in stator weight by 1.4% for each additional 2 mm of length, and the accompanying volume increase. The torque production is maintained with the increased tooth length, even though the flux path to the rotor is now slightly longer. This is attributable to high permeability of the GO-SiFe steel and the strong magnet flux component.

Both increasing the conductor aspect ratio and the teeth axial length move the conductors away from the airgap and reduce the current concentration in the conductor closest to the airgap. Fig. 4.15 shows the reduction in copper loss relative to the increase in distance between the airgap and closest conductor to the airgap. This result quantifies how the increased aspect ratio conductor is also reducing the proximity effect in the entire slot, not just next to the airgap. As well, of course, increasing the conductor aspect ratio avoids the increase in weight, volume, and core loss when increasing the stator length.

### 4.3.4 Effect of Conductor Placement

The conductor position in the slot can also be modified by increasing the space between the coil and tooth, such that the coil is more centered in the slot. This modification places the conductors closest to the airgap further away from the rotor leakage flux identified in Fig. 4.10. While this modification may increase the proximity effect between adjacent conductors in the slot, it can be seen in the original design (Fig. 4.9) that current concentration in the closet conductor to the airgap due to rotor leakage flux is much higher than that due to proximity effects. Changing the coil geometry in this way will cause an increase in DC losses since the coil wraps around a longer path which increase the wire length.

The conductor placement is modified by bringing the coils 1 mm then 2mm towards the center of the slot, as shown in Fig. 4.20. In Fig. 4.21 we can see that while the AC to DC loss ratio decreases, the total losses increase due to the increased DC loss. This approach may be of interest for machines operating at higher frequencies, if the AC loss dominates, but there is no net benefit for the considered machine. Particularly at lower speed operation the increase in total losses would be quite significant since this region is dominated by DC loss. There is also an increase in total copper weight of 3.2% and 6.4%, for relocating the coils by 1 and 2mm, respectively.

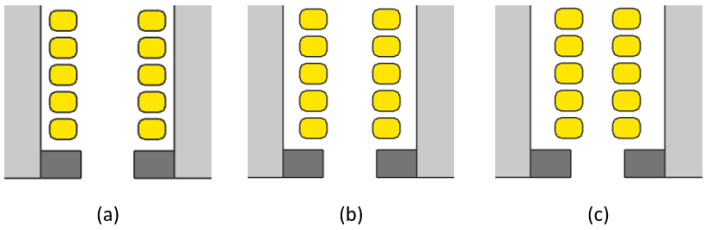


Figure 4.20: The conductor position in the slot: (a) baseline, (b) wires shifted 1 mm towards center of slot, (c) wires shifted 2 mm towards center of slot.

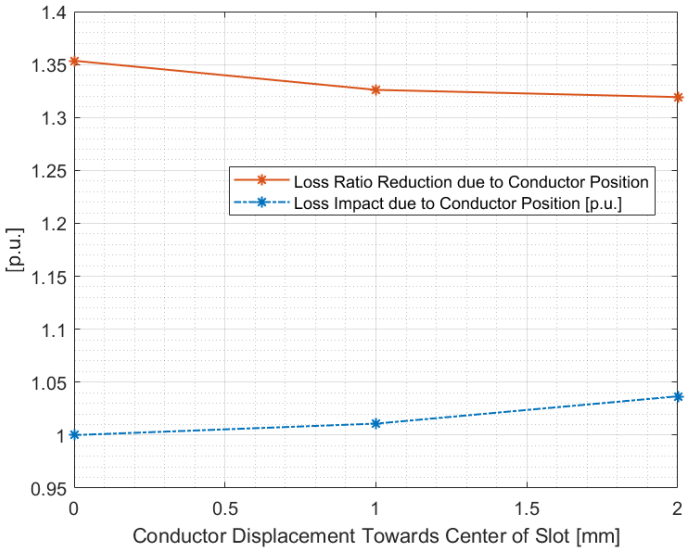


Figure 4.21: The impact of conductor position on copper loss.

### 4.3.5 Effect of Pole Shoe Design

The pole shoes control the flux path into the stator teeth. They are analogous to the tooth tips in a radial flux machine. It is manufactured of a SMC. Without pole shoes, more airgap flux passes through the coil, and flux density increases in the slot. By shaping the pole shoe, the designer can better direct rotor flux away from the coils, and limit AC losses. Here, the thickness and width of pole shoes, in addition to adding chamfers, are studied (Figs. 4.22, 4.23, and 4.27).

Fig. 4.22 shows the variation in pole thickness from 2.5 to 4.5 mm, and Fig. 4.24 shows the resultant impact on the loss ratio. If the pole shoe is too thin, there is a high level of saturation, which limits the primary torque generating flux path towards the stator tooth. As such, torque per amp decreases, and the necessary increase in excitation current increases the total copper loss. Moreover, this high saturation exacerbates the issue of rotor leakage flux cutting the corner towards the tooth. In Fig. 4.25 the saturation level in the pole shoe is about 2.2T for large areas, which is fully saturated for the SMC material, thereby reducing the material permeability to close to that of free space. As such, magnetic resistance is much more equal between the path through the shoe, and the path cutting the corner across the air gap and conductor.

On the other hand, if the pole shoe is thick, while the saturation is lower, the gap between the conductor and pole shoe is quite small, which again increases the proportion of flux impacting the conductor. The thicker pole shoe does however slightly increase torque production, and the slight reduction in excitation current reduces total copper loss. A thicker pole shoe in combination with other design modifications to move the conductor away from the airgap, can increase torque per amp and reduce overall copper loss more significantly.

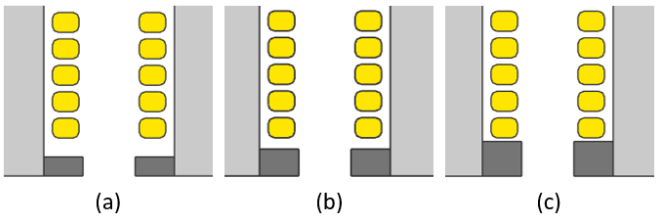


Figure 4.22: The variation of pole shoe thickness: (a) 2.5 mm pole shoe, (b) 3.5 mm baseline pole shoe, (c) 4.5 mm pole shoe.

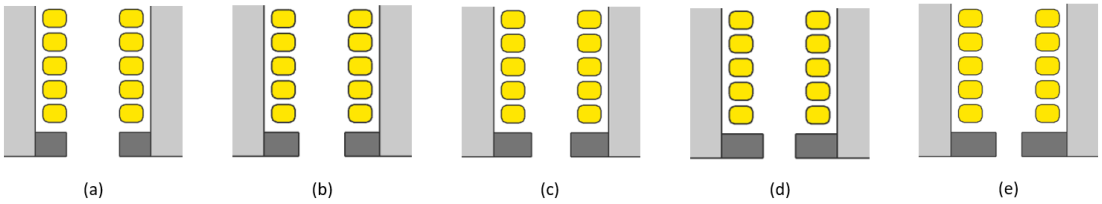


Figure 4.23: The variation of pole shoe width: (a) -0.5 mm narrower, (b) baseline, (c) 0.5 mm wider, (d) 1 mm wider, (e) 1.5 mm wider.

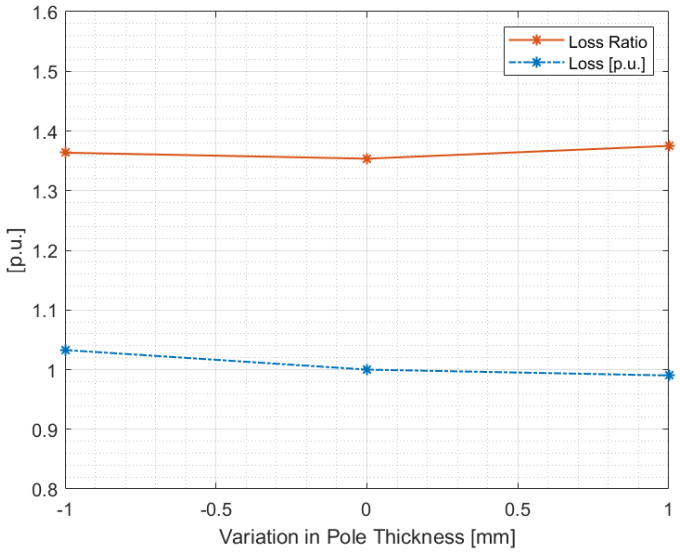


Figure 4.24: The impact of pole shoe thickness on loss ratio.

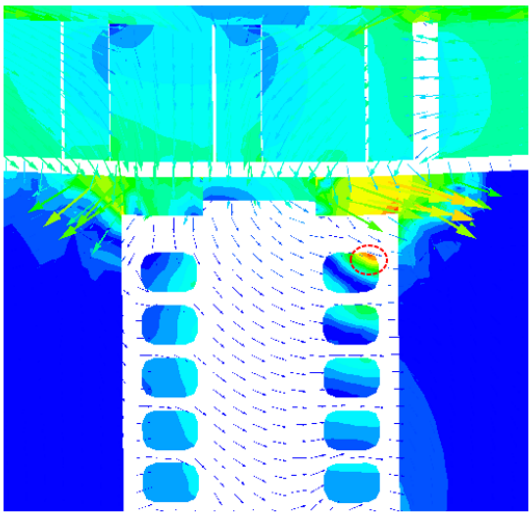

Figure 4.25: The flux field and current density in the area of concern for the 2.5mm thick pole shoe.

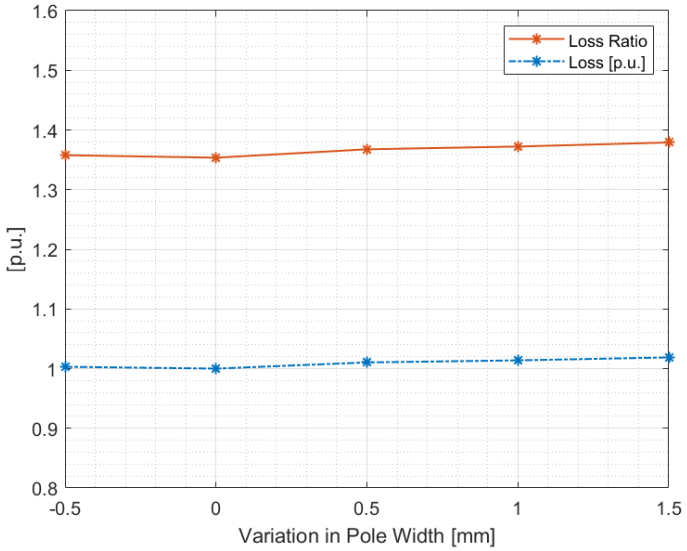


Figure 4.26: The impact of change in pole shoe width on copper loss.

The pole shoe width of the base design is optimized to enhance torque production. However, it is important to study the sensitivity of copper losses to the pole width. Increments of 0.5 mm are considered, as shown in Fig. 4.23. It is observed that the loss ratio and total loss are relatively insensitive to the pole width with a slight trend of increasing losses away from the original design, as shown in Fig. 4.26. As expected, the pole width for this machine was already well optimized in terms of torque production and changing the pole width reduces the torque per amp. As such, changing the pole width is not desired.

Instead of allowing the stray flux to "cut the corner" between the pole shoe and tooth, a chamfered pole shoe can better direct flux towards the tooth. Similar approaches have been taken in the design of tooth tips for radial flux machines [85]. A chamfer is studied on the baseline design, as well as on the 1 mm thicker pole shoe design, as shown in Fig. 4.27, with the results shown in Table 4.1. The thicker chamfered pole shoe increases the machine torque per amp, and so by reducing the excitation current, a total copper loss reduction of 5 % is possible. This design modification is inspired by the result seen with the thicker non-chamfered pole shoe, but the chamfer corrects the issue seen previously where the conductor is extremely close to the flux path within the shoe. The thicker chamfered pole shoe also has a more even saturation throughout the shoe. The chamfer on the baseline pole shoe also gives an improvement, but less than when the shoe thickness is increased.

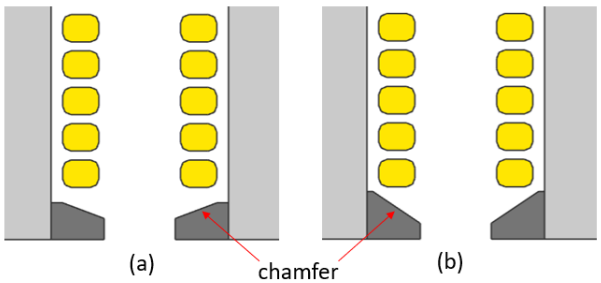


Figure 4.27: The variation in pole shoe chamfers: (a) chamfer, (b) 1mm thicker pole shoe with chamfer

Table 4.1: The Impact of Pole Chamfers on Loss.

| Modification | Loss [p.u.] | Loss Ratio |
|---|---|---|
| Original Pole Shoe | 1.0 | 1.354 |
| Chamfered Pole Shoe | 0.992 | 1.343 |
| Chamfered & 1 mm Thicker Pole Shoe | 0.950 | 1.337 |

## 4.4 Design Guidelines and Final Design

A set of design guidelines for AC loss reduction is presented. Based on this analysis, a final version of the machine is designed and simulated.

### 4.4.1 Guidelines for AC loss reduction

The following conclusions are gathered from the presented studies. These design actions should generally apply to other AFPMSMs with concentrated wound large cross-section rectangular conductors.

- Increasing the conductor aspect ratio provides considerable benefit in reducing AC copper loss, greater than other modifications that just move the conductors further away from the airgap.

- Chamfering the pole shoes helps guide the primary flux path and reduce the AC loss in the conductor closest to the airgap. In conjunction with increasing the pole shoe thickness, this modification noticeably reduces loss.

- The pole shoe width and thickness have a negligible impact on AC copper loss, whereas they directly impact the machine torque production. These parameters should be optimized to maximize machine torque per amp, and thereby reduce the excitation current and associated DC losses.

- Modifying the conductor CSA can reduce the total copper losses, but it is highly dependent on the temperature and speed operating conditions and has a direct impact on the winding weight.

### 4.4.2 Final Design

From the study of copper losses for this machine, it is clear that a high aspect ratio conductor provides considerable benefit, as well as the chamfered and thicker pole shoe. These two modifications are combined in a final design. At the nominal operating point, this design reduces total copper loss by 13.3 % , and the AC/DC loss ratio becomes 1.19. With this significant reduction in the loss ratio, it may make sense to increase the wire CSA, since this directly reduces DC copper loss. However, since this machine is for an aerospace application, the weight increase is undesirable, and the CSA is unchanged. As previously mentioned, even higher aspect ratio conductors may continue to reduce the losses in the machine. For this project, the limit was the manufacturability of such a wire, but it should be considered in other applications. Compared to the original machine presented in Chapter 2, and in combination with the torque per ampere improvement using GO-SiFe steel, the total reduction in copper loss is 16 %.

## 4.5 Chapter Summary

This study presented a series of modifications to the stator and winding geometry of the AFPMSM under study in order to reduce the total copper loss, with emphasis on understanding and reducing the AC component of this loss. The loss mechanisms that contribute to AC copper losses were identified, and examples are shown of the effect of conductor temperature and excitation frequency (motor speed). As well, the simulation methods that allow the capture of AC losses were discussed. For this study, a three dimensional FE model was employed, with multiple steps taken to reduce the element count and computational cost of the simulation. A baseline machine design was presented which has been optimized for torque production and limiting other machine losses. Working with this machine, a series of modifications were studied to reduce the total copper loss. The sensitivity of AC losses to the different modifications was evaluated. It was identified that high aspect ratio conductors, as well as pole shoe shaping in the form of chamfers, were the two most effective measures for reducing copper loss. A series of guidelines were presented that identify these two measures, as well as summarize the effectiveness of other actions. For instance, for certain machines, increasing the conductor cross section can be very valuable for reducing losses but has a significant weight penalty. Finally, an improved design was presented that sees a nearly 13 % reduction in copper losses, without any weight or performance penalties. Compared to the original machine presented in Chapter 2, the copper loss has now been reduced by 16 %.

# Chapter 5

# Design of a Compact Winding Configuration

## 5.1 Introduction

As has been discussed, one of the significant challenges of aerospace electrification is the weight and volume of the electric drive system. This chapter focuses on the winding design of an AFPMSM in order to maximize the volumetric and gravimetric power density. In Chapter 4 the wire size was chosen to minimize AC losses. Proceeding with the same machine, in order to maximize power density, care must be taken to make the winding as compact as possible. In an AFPMSM, the winding connections/terminations can go on either the outer or inner diameter (OD/ID) of the machine, giving more possibilities for the end winding configuration. In the baseline machine, the end winding connections were placed on the OD, for ease of manufacturing, and packaging. However, this left unused space at the machine ID. This chapter proposes a more compact packaging of the stator winding by utilizing this available space at the ID. In order to keep the three phase terminals accessible at the machine OD, an extra half turn is added to each phase's start coil. Non-integer coil turns can impact the stator MMF spectrum, poten-

tially impacting machine torque ripple and airgap force distribution [47]. Hence, the resultant electromagnetic impact of these coils is assessed.

Using rectangular wire imposes multiple constraints on how individual conductors can be bent to create the most compact winding [82], [86], [87]. These constraints, such as applicable wire bending and forming processes are considered. Details of the weld joints between conductors, and the welding requirements are presented. As well, the proposed design considers the wire insulation requirements and the minimum spacing between conductors, taking into account the effect of operating at altitude. This assures that the machine insulation system is free of partial discharges (PDs). Hence, the proposed winding design enables the motor to stay within its allotted volume package and meet high power density requirements, while maintaining insulation integrity.

At the end of this chapter, the proposed ID connected winding vs the OD connected winding are compared, as well as in depth analysis of the electromagnetic impact of the non-integer coil turns. These results are then discussed and conclusions are drawn for the winding design for AFPMSMS of different dimensions and power levels.

## 5.2 Machine Topology

As has been previously introduced, the considered machine has a YASA configuration, with a single stator and two rotors. Fig. 5.1 shows the motor design without the motor winding, nor the stator potting material. The coils are wound around the stator teeth as will be described in later sections. The winding connections are shown in Fig. 5.2. Each phase includes two sets of coils, where each set comprises three series-connected coils. A jumper connects the two sets, as shown in the figure. There is a neutral point where all three phases are connected. The three start coils with additional half turns are shown with an extra conductor in the slot.

## 5.3 Winding Packaging

As discussed, the winding connections of an AFPMSM can go to the OD or ID of the machine. This section discusses the benefits of each design choice. In the case of OD connections, the coil terminals come axially outwards, and the connections are made above and below the stator, as indicated by the green highlighted region of Fig. 5.3a. This concept gives clearance to the stator, and places the stator water jacket close to the winding, which is necessary for cooling. The connections are left exposed after potting the stator assembly, which simplifies the potting process because no connections need to be welded prior to potting. However, exposing the connections can reduce cooling performance since there is no direct conduction path on the surface of the conductors.

Alternatively, connections can be made at the ID of the machine. The main constraint, in this case, is the available volume at the ID, considering any components in the center of the machine. For this machine, the bearing carrier and rotor bearings limit the volume. However, it is desirable to limit the bearing diameter since smaller bearings have lower losses and a higher allowable operating speed [88]. As such, there is an annular region between the OD of the bearing carrier, and the ID of the stator coils (green highlighted in Fig. 5.3b). By taking advantage of this space to package the end winding, the motor volume is reduced, and the water jacket is able to stay similarly close to the winding. Additionally, the end connections are fully encapsulated in the potting, which improves heat transfer from the conductors. However, this configuration requires positioning and fixing in place all the end winding connections and jumpers before the potting process. Moreover, an additional half turn is required for each phase start coil to make the three-phase terminals accessible at the OD.

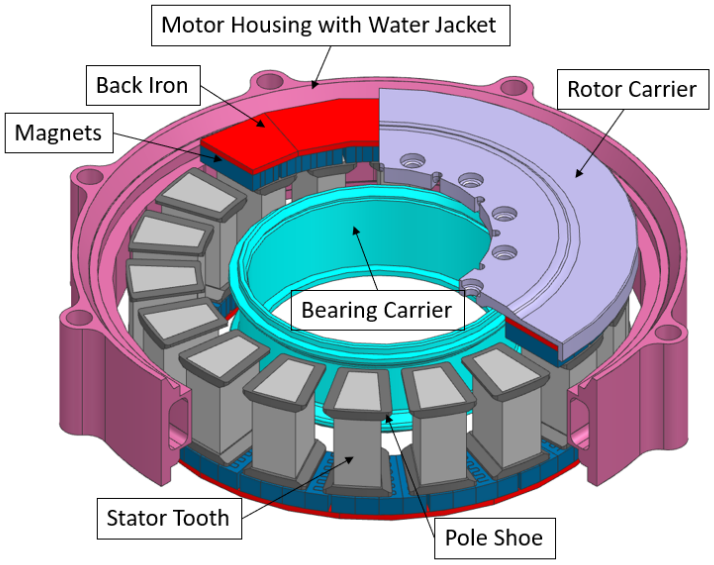


Figure 5.1: The motor assembly without the winding.

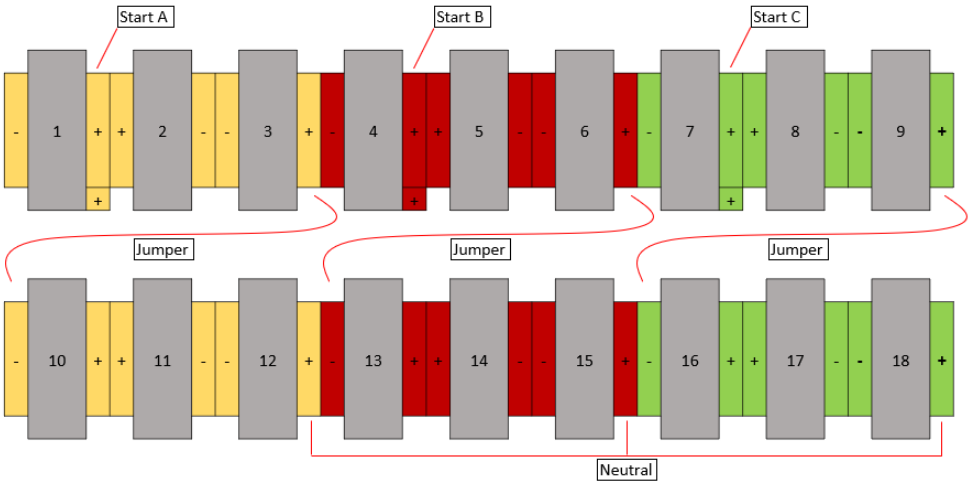


Figure 5.2: The winding scheme.

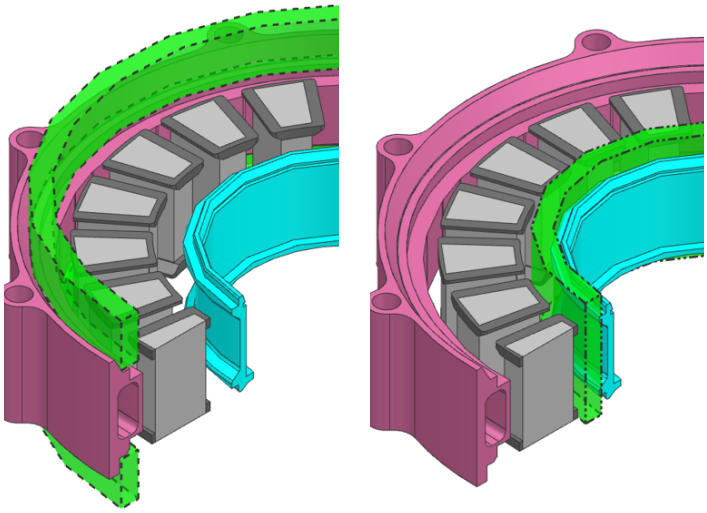

(a) (b)

Figure 5.3: The required volume for (a) OD terminations & (b) ID terminations.

## 5.4 Winding Design Constraints

### 5.4.1 Manufacturing Coils and Jumpers

Use of rectangular wire has become more prevalent in motor windings, because of compactness, high fill factor, improved machine efficiency and the possibility of automated winding and welding processes [81], [82], [86], [87]. There are two methods employed as the coils and various jumpers are manufactured: bending, and forming [89]–[91]. In the bending process, the free end of a section of wire is bent around a bending form or pin to a certain angle, most simply, in a single bending plane. This can be done multiple times to the same piece of wire to form a closed section of wire, such as the stator coils. In the forming process, the wire is pressed into a mold, and the wire deforms to match the mold shape. Care must be taken in this process not to damage the insulation as it contacts the mold [91]. Forming is often used for wires with multiple bends in multiple planes, compound curves, or long continuously curved sections. In section 5.5 the appropriate wire manufacturing process will be identified for each jumper and coil of the proposed winding.

It is often desirable to form the coils and conductors with sharp bends and complex shapes to minimize the winding volume. However, the wire has a minimum bend radius requirement to avoid damaging the copper or insulation. For the considered wire with an aspect ratio of 2.25, the minimum bend radius is 2.15 mm at the bend ID. The bending stress on the copper and insulation increases when the bend is compound, i.e., bending through multiple planes. Therefore, several simpler bends are preferable to one complex bend.

### 5.4.2 Wire Welding

Conductors are joined in the winding with a weld. Multiple weld technologies are employed for joining rectangular conductors, though in recent years, laser welding is becoming a prevalent technology because of rapid cycle times, the ability to weld closely spaced joints, and its high-quality weld joints [92]. Specifically, green lasers give cleaner welds, with reduced melted copper splatter, compared to other technologies such as infrared lasers. This is mainly attributed to the increased radiation absorption coefficient of copper at the wavelength of green lasers, therefore requiring less energy to weld [93][94].

The conductor design should consider certain constraints of the welding process, including insulation removal, fixing the joint in space, and accessibility of the joint. There is a minimum length of insulation to be removed before welding, called the strip length, which is 8 mm for the selected wire and welding process [86]. This ensures that the insulation is not damaged due to heat generated during the welding process. A similar 8 mm minimum spacing should also be respected when considering the weld joint position relative to other conductors, to prevent the heat from one weld damaging insulation on any adjacent conductors. Additionally, the wire should be oriented such that the wider faces of the wire are in contact with each other at the weld joint, which maximizes the weld strength. This is especially critical with high aspect ratio wires as are used here. In order to keep these faces in

contact, a fixture may be required to hold the conductors. Finally, the laser weld requires the joints to have a clear line of sight to the laser emitter. This is why the weld joints in the considered winding designs are oriented axially outwards.

### 5.4.3 Winding Insulation

The design of the insulation system is critical for machine reliability and durability, and ensures no winding failures. The insulation material should fulfill the motor operational requirements at the most severe working and environmental conditions. In this design, the wire is coated by PEEK, and the entire winding and stator assembly are encapsulated in epoxy. There is a layer of Nomex insulation paper between the coils and the stator teeth. The insulation system of the motor is shown in Fig. 5.4. Air voids can exist inside the potting, which resemble weak points in the insulation system and can lead to partial discharges (PDs) [95]. This happens if the voltage stress on a void exceeds the air breakdown voltage. The breakdown voltage is affected by operating conditions such as temperature and pressure [96]. This is critical in aerospace applications since the air pressure decreases with altitude.

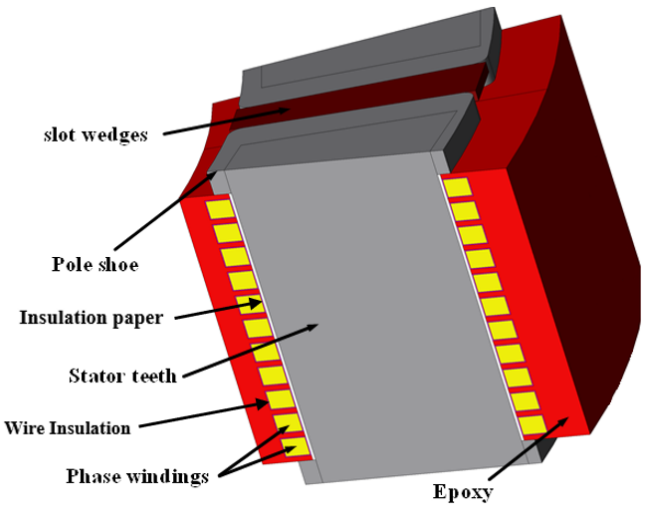


Figure 5.4: The insulation system between two teeth.

Table 5.1: The Required Minimum Spacing Between Wires

| | Min Spacing | Stress on PEEK |
|---|---|---|
| Between Phases (Coated Wire) | 0.12 mm | 2.16 kV/mm |
| Between Phases (Coated Wire passes Bare Conductor) | 0.158 mm | 1.936 kV/mm |
| Between Phases (Bare Conductors) | 0.225 mm | N/A |

The wire insulation wall thickness is defined to balance PD requirements and thermal considerations. Thicker insulation restricts heat flow into the epoxy material and towards the water jacket, whereas it increases the insulation system reliability. Therefore a minimum insulation thickness should be defined that prevents any PD activity inside the motor, even if voids exist in the epoxy. Air voids were introduced in the epoxy at different locations, and the voltage across each void was compared to the corresponding breakdown voltage for that void size, as defined by Paschen's law [97]. Paschen's law is applied since the electric field inside the voids is almost uniform due to the considerable distance between coils [98]. The calculation of insulation thickness, considering thermal aspects and maintaining a PD-free insulation system, is completed iteratively between electrostatic and thermal analyses. The final insulation thickness is defined as 0.0625 mm.

A minimum spacing (gap) needs to be kept between conductors to ensure the voltage across the gap is lower than the air breakdown voltage. The air breakdown voltage is defined by the gap thickness at the lowest expected pressure and the highest applied voltage difference between two conductors. The required minimum spacing within the winding to prevent partial discharges is presented in Table 5.1.

### 5.4.4 Phase Resistance Balance

It is important to mitigate the phase imbalance between the three phases. A large phase imbalance can cause control issue, increased torque ripple, and may increase losses in the machine [99]. Phase imbalance is primarily driven by unequal winding length between the three phases. Phase imbalance should be targeted below 5%, with a goal of reducing it as much as possible. In order to reduce excessive phase imbalance, the lengths of certain jumpers or terminal connections can be adjusted, potentially increasing the total winding length if necessary. Another possible option is to use conductors with larger or smaller cross sectional area to increase or decrease resistance in sections of the end winding for one phase but not the others.

## 5.5 Detailed Winding Design Procedure

The wound coil is an 11-turn trapezoidal helix spaced 0.65 mm away from the stator tooth. This spacing is defined based on the manufacturing tolerance of the coil and tooth, plus accounting for a 0.2 mm slot liner. The trapezoidal shape is made by four consecutive bends, with a 2.15 mm bend radius. The helix is defined by an axial spacing of 0.725 mm between turns, or layers, which evenly spaces the turns along the axial length of the tooth. This spacing also leaves room for epoxy potting to flow between turns. The transition between turns is achieved by bending up the beginning of the next turn, before the next trapezoidal section is bent. This causes compound bending (twist) in the wire, which is usually undesirable, but the twist is relatively minor, and the alternative forming process for each coil turn is significantly more complex to manufacture. The coil features are identified in Fig. 5.5.

The coils with the additional half turn have the same helix form. However, the start point and the twist between turns happens at the outer surface of the coil, closest to the stator housing, instead of at the ID. The last turn of this coil, instead of terminating at the OD, is wrapped around the tooth one additional time, passing back through the stator slot, as shown in Fig. 5.5. The additional half turn increases the axial height of this coil slightly. Both types of coils would be wound on a separate mandrel before being placed over the stator tooth.

Adjacent coils are joined directly, instead of using separate jumpers. The terminal of each coil is extended radially inwards, then bent towards its mating wire, as shown in Fig. 5.5. Where the two coils meet, the terminals are bent axially outwards to make a joint for welding. In the joint design, enough length is given to allow for 8 mm of stripped length, as recommended for welding. The coil terminations are also designed such that conductors meet on the wider face, maximizing the width of the weld joint and forming a stronger weld. The tip of the weld joint also meets the requirement of being 8 mm away from other conductors in the coil.

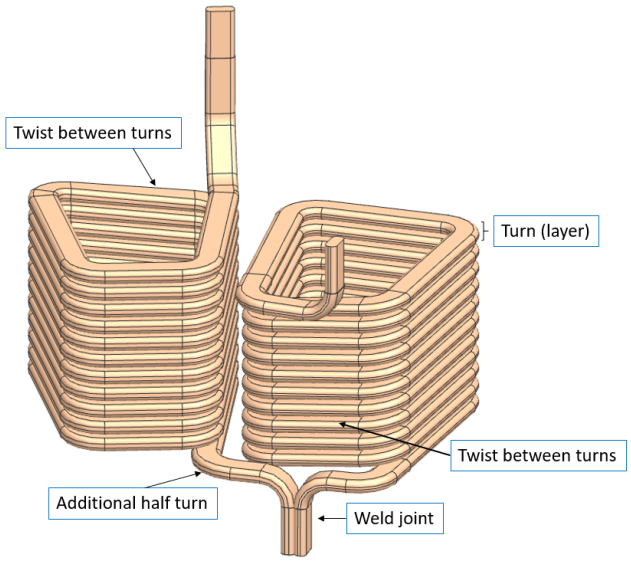


Figure 5.5: Two adjacent coils with a weld joint.

Once all the adjacent coil connections are complete, the neutral point of the winding is designed. The neutral point is made by connecting the end-points of phase A and C to the end-point of phase B using two jumpers, as shown in Fig. 5.6, with the jumpers highlighted. Since these connections are not adjacent, the jumpers must pass by other weld joints. This can be done by bringing the jumper above, below, or radially inward of, the other weld joint. Since the available radial space is limited by the bearing support, passing radially inwards is not possible. Likewise, bringing the jumper upwards over the weld joint would interfere with the rotor, and impede the welding process. Bringing the jumper below the adjacent hairpins and then up to meet the neutral point is the simplest solution, and respects the necessary 8mm clearance around any weld joint. A weld across three conductors, shown in Fig. 5.6, forms the machine neutral point. In terms of manufacturing, the neutral jumper is a formed wire because of the continuous curved section as it passes along the circumference of the ID.

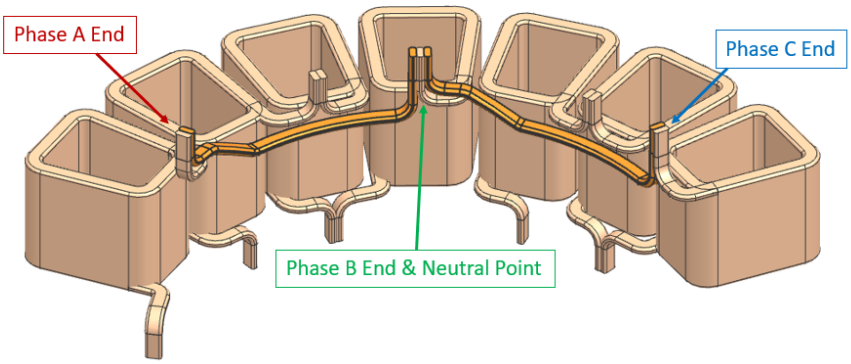


Figure 5.6: The neutral jumpers and neutral point.

The phase jumpers connect two sets of three coils to form the six series-connected coils per phase. Since the start point of the phase C jumper is before the endpoints of the phase A and phase B jumpers, conductors have to pass each other. This is done in the least possible space by minimizing the number of crossing points and reducing the overlap where two conductors pass. Moreover, in order to limit cost and complexity, the jumpers should be identical. The design of three jumpers, including how they cross over each other, is shown in Fig. 5.7. Moving clockwise, the phase A jumper rises over the phase B jumper, keeping both wires at the same diameter. It then jogs radially inwards, forming the crossover point between phase A and phase B jumpers. Finally, it is terminated by bringing the wire back down axially and jogging radially outwards. A similar pattern applies to phase B and phase C jumpers. The crossover point is the lowest clearance point in the winding, with a separation of 1.08 mm. This is well above the minimum clearance of 0.12 mm required for insulation integrity, however, a positional tolerance on conductors of 0.3-0.5 mm makes this gap necessary. Plastic spacers are added to help ensure the gap is maintained in the winding assembly. This jumper design is key to the feasibility of the compact winding, and must be manufactured with precision. The phase jumper is manufactured using both forming and bending, because of the long continuously curved section and complex bend geometry at the termination. The overall winding design is presented in Fig. 5.8.

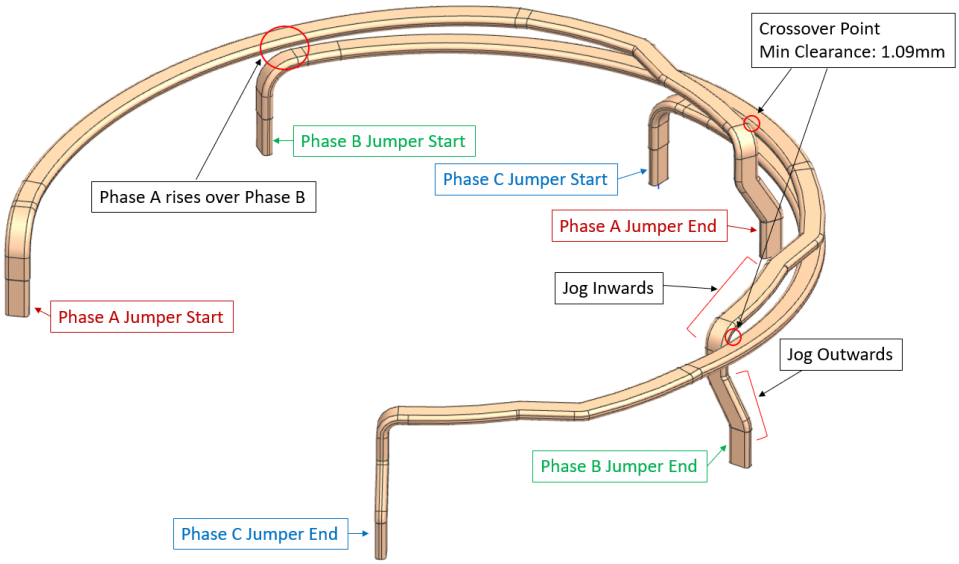


Figure 5.7: The phase jumper.

The proposed winding has a phase imbalance of 1.9%. This is caused by the neutral point being formed at the weld joint of the end of phase B. The neutral jumper from phase A and C add to the resistance of those phases. However, this phase imbalance is deemed acceptable.

## 5.6 Comparison Between ID-Terminated and OD-Terminated Windings

This study seeks to define the best approach for winding an axial-flux machine with rectangular conductors. A comparison between the proposed design and a design with OD terminations is presented. It is initially intuited that ID terminations provide the best packaging solution, but the results quantify the compactness of the proposed design.

A brief summary of the OD-terminated winding design is presented. The coils are similar to that of the ID-terminated winding coils, but the coil terminals face the stator OD rather than the ID. A small jumper is used to join coils instead of having the coil terminals turn and meet directly. This is because the distance from

one terminal to the next is larger at the stator OD. The phase jumpers between two sets of three coils are similar to the ID-terminated design, with two crossover points. Finally, the neutral jumpers connects phase A and C to phase B, and similar to the ID-terminated winding, must pass around adjacent weld joints. The overall OD-terminated winding is presented in Fig. 5.9. Note that the end winding region is split by orienting the weld joints axially outwards, in order to leave space for the motor housing and water jacket.

The coil volume of the two windings is the same, so only the end winding volume is compared to assess each winding's compactness. The end winding volume is defined as the volume of an annular region of rectangular cross-section encompassing all conductors in the end winding. This region does not include the coils, or the three-phase leads. The total end winding volume is 252.8 $cm^3$ and 345.1 $cm^3$ for the ID-terminated and OD-terminated windings, respectively. The ID end winding is approximately 28% smaller than the OD one. The end winding volume of the OD-terminated winding also directly contributes to the overall volume of the machine, whereas the ID terminations fit into an otherwise unused space. Moreover, the ID-terminated winding shows better thermal performance because the end winding is encapsulated in the potting material, which is not possible with the exposed OD terminations. Finally, in terms of total wire length, the ID-terminated winding is 5.3% shorter, corresponding to a further 5.3% reduction in DC copper loss compared to the result in chapter 4. Overall, in conjunction with the previous actions, the total copper loss has been reduced by over 20 %. The benefits of the ID terminated winding would be beneficial for other size AFPMSMs as well, with the greatest benefit expected when the ratio of stator OD to ID is large.

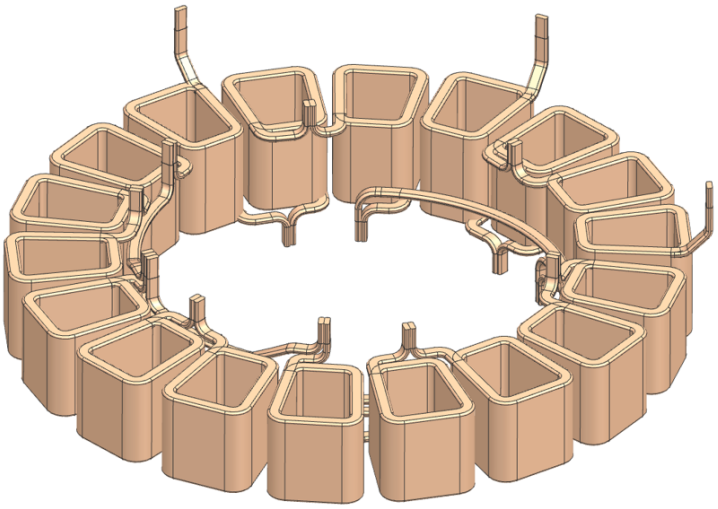

Figure 5.8: The proposed ID-terminated winding.

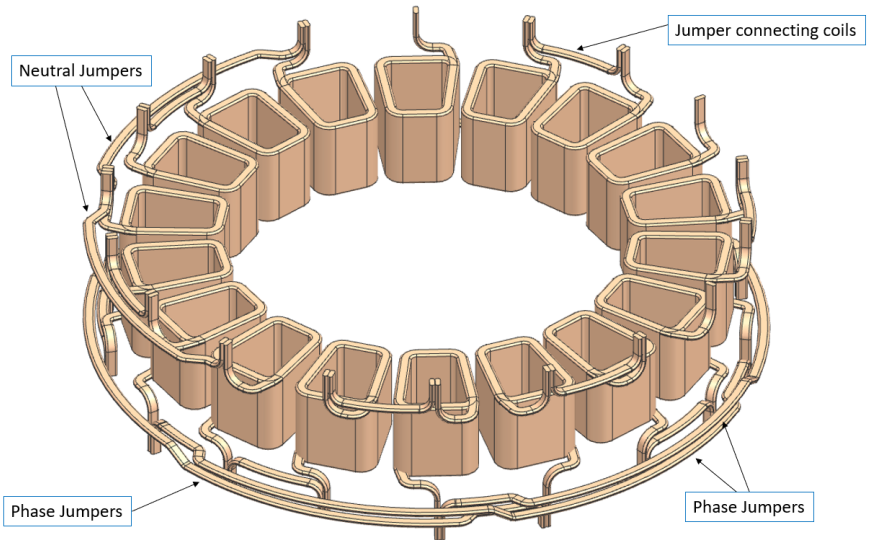


Figure 5.9: The OD-terminated winding.

## 5.7 Electromagnetic Analysis of ID-Terminated Winding

Although the proposed winding shows a clear packaging benefit, it could introduce an imbalance in the electromagnetic design due to the additional half turns. Hence, the effect of the additional half turns needs to be quantified. A full 3-D FE model is built to capture the winding asymmetry [100]. The 11-turn coils are modeled in a bulk coil representation, whereas the 11.5-turn coils are modeled in detail, placing the extra conductor in the appropriate slot.

Fig. 5.10 compares the torque and torque ripple of the proposed machine and the same machine without additional half turns over one electrical cycle at the base speed operating point. The average torque increases by 1.6 % and the torque ripple is reasonable at approximately 4 %. Magnet and and iron losses were unaffected. Fig. 5.11 shows the normalized airgap flux along a line in the middle of the airgap, around the circumference of the machine, for a single point in time, comparing between the machine with and without additional half turns. Then, Fig. 5.12 shows the spatial harmonic distribution of Fig. 5.11. In this analysis, the machine is simulated with a non-magnetized rotor to study only the flux contribution from the excited stator winding. It can be seen in Fig. 5.11 that there are slight variations in airgap flux, however there is no significant change in the harmonic distribution of both machines. The values in both Figs. 5.10, 5.11, and 5.12 are normalized based on the values of the machine without the additional half turns.

Axial tooth force is also studied since the uneven distribution of coils with additional half turns may cause unbalanced forces on the rotor. Fig. 5.13 shows the tooth forces within the proposed machine for one tooth wound with an additional half turn, and the opposing tooth wound with 11 turns, for one electrical cycle. The peak axial forces remain balanced between the two teeth, however, there is

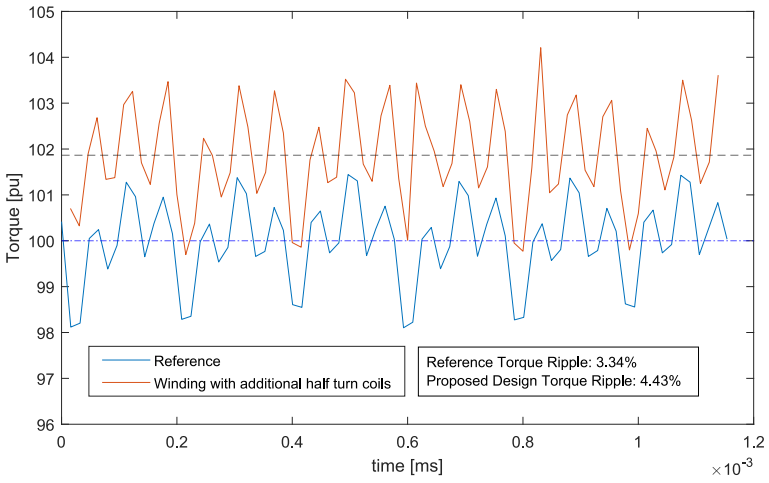


Figure 5.10: The electromagnetic torque versus time characteristics.

a slight increase in peak tangential force acting on the tooth with the additional half turn. This can be explained by studying the rotor position at the time of peak axial and tangential forces. When the magnet pole is aligned with the stator tooth, the axial force is at its peak, and this axial force is dominated by the permanent magnet flux. At the peak tangential force, the magnet pole is offset from the stator tooth, generating higher tangential forces, and the stator tooth coil is at its peak excitation. Therefore, as compared to the peak axial force, a more significant proportion of the air gap flux is generated by the stator excited coils. The increased tangential force corresponds with the slight increase in rotor torque for the machine with the additional half turns. Overall, the variations in tooth forces are not significant enough to cause concern with respect to unbalanced forces on the rotor.

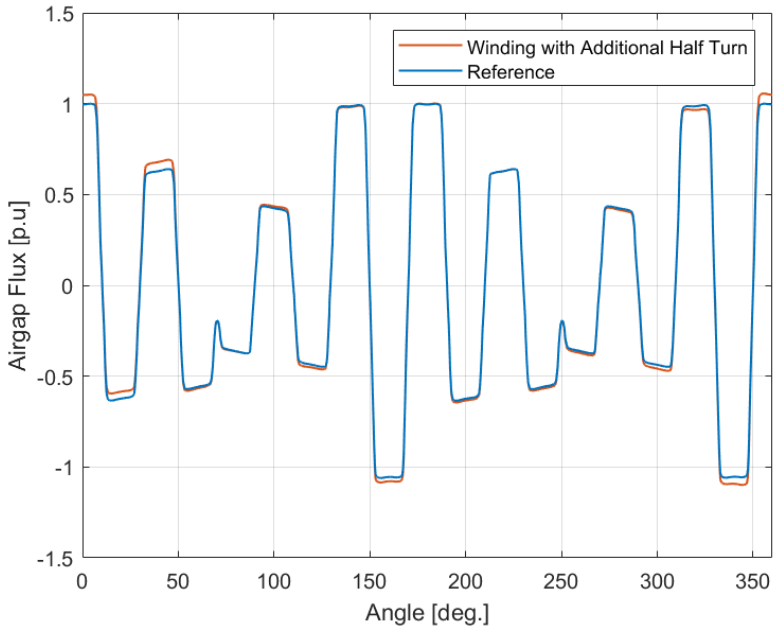


Figure 5.11: The axial component of stator airgap flux density around the circumference of the machine.

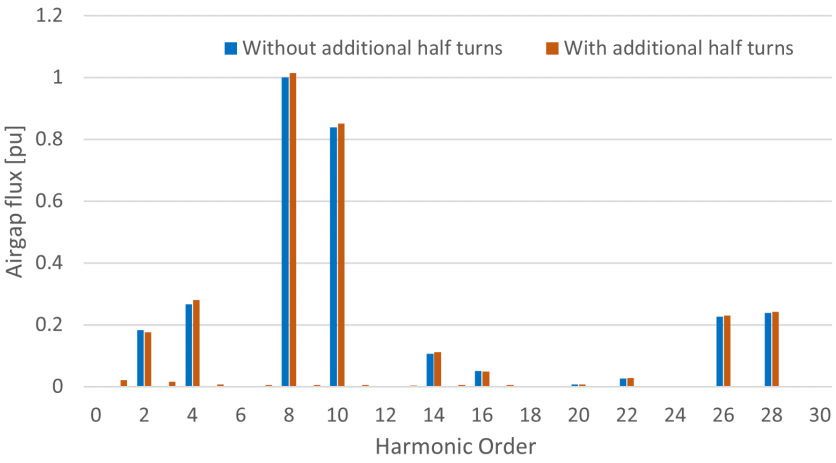


Figure 5.12: The FFT spectrum of the axial component of stator airgap flux density.

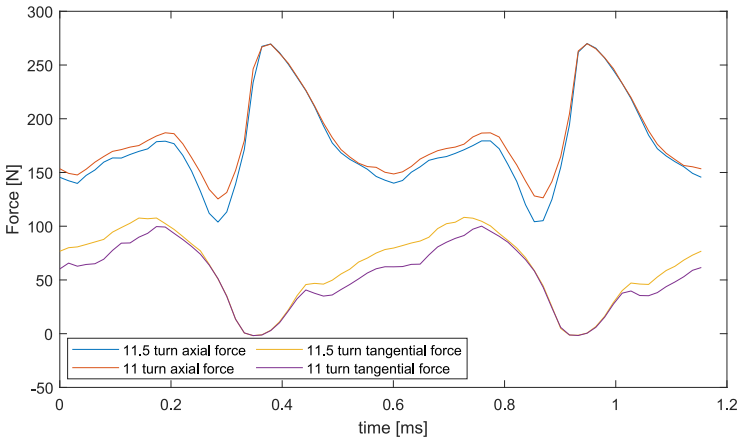


Figure 5.13: The tooth forces versus time characteristics.

## 5.8 Chapter Summary

This chapter proposed a detailed winding design procedure of an AFPMSM for an aerospace application. Building upon the work of the previous chapters, the winding design completes the overall stator design. ID winding terminations were employed to minimize the winding volume. Additional half turns were added to the start coils of the phases to place the three-phase terminals at the machine OD. The winding design and insulation constraints were identified, and the manufacturing methods were discussed. These constraints and methods are general, and apply to other similar concentrated wound machines. Then the proposed design was compared with the OD-terminated winding design to quantify the compactness and significance of the ID-terminations. The ID-terminated winding is 30 % smaller in volume, and uses 5.3 % less copper than the original OD-terminated design. This reduction in wire length further contributes to loss reduction in the stator. In combination with the increased torque per ampere of the material choice, and the reduction in AC copper loss, the total reduction in copper loss relative to the first introduced design is 19.8 %. Finally, the electromagnetic impact of the additional half turns employed in the ID-terminated winding was assessed. It was found that the torque is slightly increased, the torque ripple was maintained at

an acceptable level, and there was only a slight change in the tooth forces within the machine. Hence, the proposed ID-terminated winding ensures the compactness of the stator winding in high power density AFPMSMs while not causing any significant adverse effects on the machine electromagnetic performance. This concept of the ID-terminated winding has broad applicability to other AF machine designs, particularly for aerospace or other applications where power density is of high importance.

# Chapter 6

# Conclusions and Future Work

## 6.1 Conclusion

Global aviation has been one the great innovations of the last century, linking people around the globe, and speeding the transit of goods and people everywhere. However, as the world confronts the growing impact of climate change, emissions must be reduced. Aviation contributes an ever growing percentage of global emissions. As discussed in the introduction, air travel is expected to triple in the next 30 years [2].

One of the primary technological solutions to be leveraged in reducing emissions is aircraft electrification. The MEA and electrically propulsed aircraft were introduced. While MEA are beginning to be adopted in commercial aviation, electric propulsion faces further technical challenges to large scale adoption. Factors identified were the power density, reliability and fault tolerance of the electric drive, as well as power density of batteries. In this project, a compact and high power AFPMSM electric drive is being developed for an electric aircraft. The primary objective of this thesis was to improve the stator design of the AFPMSM by reducing loss, weight, and volume.

In Chapter 2 electric machines in MEA, and electric propulsion were reviewed and it was shown that an AFPMSM is an attractive choice. The machine under

study was then introduced, reviewing electromagnetic, mechanical, and thermal design of an AFPMSM. Simulation methods for an AFPMSM were also introduced. A three-dimensional FE method was chosen as the primary simulation tool. Due to the high computational load of the model, methods for reducing simulation time were employed. These include taking advantage of model symmetries, meshing techniques, and a hybrid model for calculation of total copper loss.

The following chapters targeted three actions to meet the objectives for the stator: choosing the optimal material for the stator teeth, AC copper loss reduction by geometry modification, and volume reduction by implementing a novel winding design. Chapter 3 presented a study of soft magnetic materials in the stator. After reviewing magnetic materials in electric machines for aerospace, four materials were selected for comparison; NO-SiFe, GO-SiFe and CoFe electrical steel, and SMC. After considering manufacturing and cost constraints, and performance with the different materials, NO-SiFE and GO-SiFe were the most competitive options. GO-SiFe, with its superior magnetic properties along the grain direction of the material, has seen application in other YASA AFPMSMs with positive results [63], [64]. The results here agree with the finding that GO-SiFe steel has noticeably better torque per ampere than NO-SiFe, but core loss was actually found to increase. However, when comparing overall losses, the machine using GO-SiFe steel had only slightly higher losses, and about 4 % reduced copper loss, due to the lower excitation current. This reduced the thermal stress in the winding, which is the hottest point in the machine. For this reason GO-SiFe was selected.

In Chapter 4 copper loss was further reduced by modifying the stator and wire geometry. The beginning of this chapter introduced the origins of AC copper loss, primarily identifying two leakage flux effects, named as proximity effect and rotor leakage flux, that contribute to AC loss in this machine. Case studies at different operating conditions illustrated the AC loss dependence on temperature and excitation frequency. In order to reduce AC loss, a series of modifications to the wire geometry, coil geometry, and stator tooth and pole shoe were proposed. In

studying the wire size, it was realized that increasing or decreasing the wire cross section area was a trade off of DC loss versus AC loss. Further study showed that at different temperature or excitation frequencies (speed) the ideal wire size would change. Other modifications directly targeted AC loss. It was found that high aspect ratio wire, and a compressed coil such that the wire was placed further away from the airgap, was highly effective at reducing AC loss. Additionally, increasing the pole shoe thickness while adding a chamfer better directed rotor leakage flux away from the wires, and increased torque per ampere in the machine. Similarly to the conclusion of chapter 3, this allowed for a reduction in excitation current, which reduced copper loss. Combined, these actions reduced total copper loss by a further 13 %.

With the wire, coil, and stator geometry defined, focus was placed on the overall winding design, specifically the packaging of the end terminations. While the three phase connections must stay on the OD of the machine to connect to the inverter, the other terminations can be placed on the OD or ID of the machine. In chapter 5 a novel ID terminated winding was proposed to the reduce the overall volume of the winding, with additional half turns on the start coils to place the three phase connections on the OD. Constraints to the design, like manufacturing limits, welding requirements and electrical insulation requirements were defined. To ensure insulation integrity, minimum spacing between conductors was calculated from an electrostatic analysis. After presenting the detailed design of the ID terminated winding, it was compared to a previously designed OD terminated winding. Overall winding volume was reduced by approximately 30 %, 5 % less copper was used, and DC copper loss dropped by a corresponding 5 %. Finally, this novel winding was also analyzed electromagnetically, since the unevenly spaced additional half turns can unbalance the magnetic circuit. However, in this case, it was shown that the harmonic distribution in the airgap was only marginally different. Torque actually increased slightly, and torque ripple and tooth forces were maintained within an acceptable limit.

As compared to the baseline model presented in Chapter 2, the improved machine has successfully met the objectives set out for the project. The stator volume and weight were reduced significantly by utilizing an ID-terminated winding. The overall machine losses were reduced by 8 %, including a 20 % reduction in copper loss, which significantly improved the thermal performance. The improved machine is more compact, lighter, and more efficient.

## 6.2 Future Work

In terms of future work, there are a few paths of interest. The first is to focus on experimental validation of the results. A primary study required would be further material testing of grain oriented steel. As was discussed in Chapter 3, the test data for the utilized steel showed non-linearity that did not match well with the core loss model. This was especially the case for high frequency, where the available test data was sparse. Further work focused on high frequency, as well as high saturation level core loss testing of GO steel at all flux angles relative to the grain should improve the loss estimate, and strengthen confidence in the material choice. Additionally, entire machine validation is necessary, particularly to validate the machine efficiency. The use of the three-dimensional FE model has been shown to be accurate for an AFPMSM, however experimental verification is important. This work can also focus on the separation of loss components in experimental data. This is complex topic, and further research can be conducted on experimental methods to for instance separate the contributions of copper loss versus iron loss in an AFPMSM, in a range of operating conditions.

For further design improvements, future work would be to take the ID-terminated winding and develop a manufacturing system for mass production. While there was a focus on manufacturability in this study, additional focus could be placed on cost and manufacturing time. Similarly, utilizing higher aspect ratio wire in order to further reduce AC copper loss was not possible due to manufacturing

constraints in this project. Those with expertise in coil manufacturing may be interested to further develop this work and develop thin, flat, conductors that can employed in YASA AFPMSMs, or other concentrated wound machines.

Finally, it would be of interest to apply the findings from this study to other axial flux machines. Optimal solutions were proposed for this machine, and its primary operating condition. Other applications may see different sensitivities to the recommended design modifications. Particularly the study on optimal wire size in Chapter 4 may have a different solution for other machines, or applications. Studies on other machines can help to generalize this work, and create a series of design recommendations useful to a wider range of machine designers.

# References


[1] B. Graver, K. Zhang, and D. Rutherford, "$Co_2$ emissions from commercial aviation, 2018," The International Council on Clean Transportation, Tech. Rep., Sep. 2019.

[2] ICAO, "Icao global environmental trends – present and future aircraft noise and emissions, working paper 54," International Civil Aviation Organization, Tech. Rep., 2019.

[3] P. Wheeler and S. Bozhko, "The more electric aircraft: Technology and challenges.," *IEEE Electrification Magazine*, vol. 2, no. 4, pp. 6–12, 2014.

[4] N. Cumpsty, D. Mavris, and M. Kirby, "Icao environmental report 2019 (chapter 1 – aviation and the environment: Outlook)," International Civil Aviation Organization, Tech. Rep., 2019.

[5] C. Gerada, M. Galea, and A. Kladas, "Electrical machines for aerospace applications," in *Proc. 2015 IEEE Workshop on Electrical Machines Design, Control and Diagnosis (WEMDCD)*, 2015, pp. 79–84.

[6] D. Fedy, *Harbour air, magnix join forces with h55 to certify world's first all-electric commercial airplane*, May 2021. [Online]. Available: `https://skiesmag.com/news/harbour-air-magnix-join-forces-h55-certify-first-electric-commercial-airplane/`.

[7] Rolls-Royce, *Accel: Entering the era of zero-emissions aviation*, May 2021. [Online]. Available: `https://www.rolls-royce.com/innovation/accel.aspx#motors`.

[8] Airbus, *Electric flight*, Jun. 20, 2021. [Online]. Available: `https://www.airbus.com/innovation/zero-emission/electric-flight`.

[9] R. Jones, "The more electric aircraft: The past and the future?" In *Proc. IEE Colloquium on Electrical Machines and Systems for the More Electric Aircraft (Ref. No. 1999/180)*, 1999, pp. 1/1–1/4.

[10] W. Cao, B. C. Mecrow, G. J. Atkinson, J. W. Bennett, and D. J. Atkinson, "Overview of electric motor technologies used for more electric aircraft (mea)," *IEEE Trans. on Industrial Electronics*, vol. 59, no. 9, pp. 3523–3531, 2012.

[11] P. Mahvelatishamsabadi and A. Emadi, "Electric propulsion system for exceptionally short takeoff and landing electric air vehicles," *IEEE Trans. on Transportation Electrification*, vol. 6, no. 4, pp. 1562–1576, 2020.

[12] M. Sinnet, "787 no-bleed systems: Saving fuel and enhancing operational efficiencies," *Aero Quarterly*, pp. 6–11, 2007. [Online]. Available: `https://www.boeing.com/commercial/aeromagazine/articles/qtr_4_07/article_02_1.html`.

[13] F. R. Ismagilov, V. Y. Vavilov, V. V. Ayguzina, I. Petrov, and J. Pyrhönen, "100-kw high-speed electric motor for the air conditioning system of more electric aircrafts," in *Proc. 2020 Int. Conf. on Electrical Machines (ICEM)*, vol. 1, 2020, pp. 559–564.

[14] J. Li, Z. Yu, Y. Huang, and Z. Li, "A review of electromechanical actuation system for more electric aircraft," in *Proc. 2016 IEEE Int. Conf. on Aircraft Utility Systems (AUS)*, 2016, pp. 490–497.

[15] J. Rosero, J. Ortega, E. Aldabas, and L. Romeral, "Moving towards a more electric aircraft," *IEEE Aerospace and Electronic Systems Magazine*, vol. 22, no. 3, pp. 3–9, 2007.

[16] K. Emadi and M. Ehsani, "Aircraft power systems: Technology, state of the art, and future trends," *IEEE Aerospace and Electronic Systems Magazine*, vol. 15, no. 1, pp. 28–32, 2000.

[17] L. P. Di Noia and R. Rizzo, "Design of a five-phase permanent-magnet motor for the electric steering of an aircraft nose landing gear," *IET Electrical Systems in Transportation*, vol. 7, no. 4, pp. 327–333, 2017.

[18] S. Ullah, S. P. McDonald, R. Martin, M. Benarous, and G. J. Atkinson, "A permanent magnet assist, segmented rotor, switched reluctance drive for fault tolerant aerospace applications," *IEEE Trans. on Industry Applications*, vol. 55, no. 1, pp. 298–305, 2019.

[19] M. Tursini, M. Villani, G. Fabri, and L. Di Leonardo, "A switched-reluctance motor for aerospace application: Design, analysis and results," *Electric Power Systems Research*, vol. 142, pp. 74–83, 2017.

[20] J. Bennett, D. Mecrow B.C.and Atkinson, and G. Atkinson, "Safety-critical design of electromechanical actuation systems in commercial aircraft," *IET Electric Power Applications*, vol. 5, 37–47(10), 1 Jan. 2011.

[21] C. Gerada and K. J. Bradley, "Integrated pm machine design for an aircraft ema," *IEEE Trans. on Industrial Electronics*, vol. 55, no. 9, pp. 3300–3306, 2008.

[22] C. Ferreira, S. Jones, W. Heglund, and W. Jones, "Detailed design of a 30-kw switched reluctance starter/generator system for a gas turbine engine application," *IEEE Trans. on Industry Applications*, vol. 31, no. 3, pp. 553–561, 1995.

[23] D. Powell, G. Jewell, D. Howe, and K. Atallah, "Rotor topologies for a switched-reluctance machine for the 'more-electric' aircraft engine," *IEE Proceedings - Electric Power Applications*, vol. 150, 311–318(7), 3 May 2003.

[24] O. Bottauscio, G. Serra, M. Zucca, and M. Chiampi, "Role of magnetic materials in a novel electrical motogenerator for the more electric aircraft," *IEEE Trans. on Magnetics*, vol. 50, no. 4, pp. 1–4, 2014.

[25] F. Bu, H. Liu, W. Huang, *et al.*, "Induction-machine-based starter/generator systems: Techniques, developments, and advances," *IEEE Industrial Electronics Magazine*, vol. 14, no. 1, pp. 4–19, 2020.

[26] G. Rizzoli, G. Serra, P. Maggiore, and A. Tenconi, "Optimized design of a multiphase induction machine for an open rotor aero-engine shaft-line-embedded starter/generator," in *Proc. IECON 2013 - 39th Annual Conference of the IEEE Industrial Electronics Society*, 2013, pp. 5203–5208.

[27] Y. Wang, S. Nuzzo, H. Zhang, W. Zhao, C. Gerada, and M. Galea, "Challenges and opportunities for wound field synchronous generators in future more electric aircraft," *IEEE Trans. on Transportation Electrification*, vol. 6, no. 4, pp. 1466–1477, 2020.

[28] MagniX, *Products*, May 27, 2021. [Online]. Available: `https://www.magnix.aero/products`.

[29] G. V. Brown, A. F. Kascak, B. Ebihara, *et al.*, "Nasa glenn research center program in high power density motors for aeropropulsion," National Aeronautics and Space Administration Cleveland, Tech. Rep., 2005.

[30] P. J. Masson, J. E. Pienkos, and C. A. Luongo, "Scaling up of hts motor based on trapped flux and flux concentration for large aircraft propulsion," *IEEE trans. on applied superconductivity*, vol. 17, no. 2, pp. 1579–1582, 2007.

[31] C. A. Luongo, P. J. Masson, T. Nam, *et al.*, "Next generation more-electric aircraft: A potential application for hts superconductors," *IEEE Trans. on applied superconductivity*, vol. 19, no. 3, pp. 1055–1068, 2009.

[32] J. E. Pienkos, P. J. Masson, S. V. Pamidi, and C. A. Luongo, "Conduction cooling of a compact hts motor for aeropropulsion," *IEEE trans. on applied superconductivity*, vol. 15, no. 2, pp. 2150–2153, 2005.

[33] P. J. Masson and C. A. Luongo, "Hts machines for applications in all-electric aircraft," in *Proc. 2007 IEEE Power Engineering Society General Meeting*, IEEE, 2007, pp. 1–6.

[34] A. El-Refaie and M. Osama, "High specific power electrical machines: A system perspective," in *Proc. 2017 20th Int. Conf. on Electrical Machines and Systems (ICEMS)*, 2017, pp. 1–6.

[35] YASA, *750r electric motors*, May 2021. [Online]. Available: `https://www.yasa.com/wp-content/uploads/2018/01/YASA-750-Product-Sheet.pdf`.

[36] M. Galea, Z. Xu, C. Tighe, T. Hamiti, C. Gerada, and S. Pickering, "Development of an aircraft wheel actuator for green taxiing," in *Proc. 2014 Int. Conf. on Electrical Machines (ICEM)*, 2014, pp. 2492–2498.

[37] A. Mitcham and J. Cullen, "Permanent magnet generator options for the more electric aircraft," in *Proc. 2002 Int. Conf. on Power Electronics, Machines and Drives (Conf. Publ. No. 487)*, 2002, pp. 241–245.

[38] F. R. Ismagilov, L. Papini, V. E. Vavilov, and D. V. Gusakov, "Design and performance of a high-speed permanent magnet generator with amorphous alloy magnetic core for aerospace applications," *IEEE Trans. on Industrial Electronics*, vol. 67, no. 3, pp. 1750–1758, 2020.

[39] T. Zhao, S. Wu, and S. Cui, "Multiphase pmsm with asymmetric windings for more electric aircraft," *IEEE Trans. on Transportation Electrification*, vol. 6, no. 4, pp. 1592–1602, 2020.

[40] S. Wu, C. Tian, W. Zhao, J. Zhou, and X. Zhang, "Design and analysis of an integrated modular motor drive for more electric aircraft," *IEEE Trans. on Transportation Electrification*, vol. 6, no. 4, pp. 1412–1420, 2020.

[41] P. J. Masson, P. Tixador, and C. A. Luongo, "Safety torque generation in hts propulsion motor for general aviation aircraft," *IEEE Trans. on Applied Superconductivity*, vol. 17, no. 2, pp. 1619–1622, 2007.

[42] T. Woolmer and M. McCulloch, "Analysis of the yokeless and segmented armature machine," in *Proc. 2007 IEEE Int. Electric Machines Drives Conference*, vol. 1, 2007, pp. 704–708.

[43] P. B. Reddy, A. M. EL-Refaie, and K.-K. Huh, "Effect of number of layers on performance of fractional-slot concentrated-windings interior permanent magnet machines," *IEEE Trans. on Power Electronics*, vol. 30, no. 4, pp. 2205–2218, 2015.

[44] F. G. Capponi, G. De Donato, G. A. Rivellini, and F. Caricchi, "Fractional-slot concentrated-winding axial-flux permanent-magnet machine with tooth-wound coils," in *Proc. 2012 XXth Int. Conf. on Electrical Machines*, 2012, pp. 281–287.

[45] F. Magnussen and C. Sadarangani, "Winding factors and joule losses of permanent magnet machines with concentrated windings," in *Proc. IEEE Int. Electric Machines and Drives Conference, 2003. IEMDC'03.*, vol. 1, 2003, 333–339 vol.1.

[46] Emetor, *Electric motor winding calculator*, Jun. 12, 2021. [Online]. Available: `https://www.emetor.com/windings/`.

[47] G. Dajaku and D. Gerling, "Eddy current loss minimization in rotor magnets of pm machines using high-efficiency 12-teeth/10-slots winding topology," in *Proc. 2011 Int. Conf. on Electrical Machines and Systems*, 2011, pp. 1–6.

[48] X. Zhang, C. L. Bowman, T. C. O'Connell, and K. S. Haran, "Large electric machines for aircraft electric propulsion," *IET Electric Power Applications*, vol. 12, 767–779(12), 6 Jul. 2018.

[49] N. Taran, V. Rallabandi, D. M. Ionel, G. Heins, and D. Patterson, "A comparative study of methods for calculating ac winding losses in permanent magnet machines," in *Proc. 2019 IEEE Int. Electric Machines Drives Conference (IEMDC)*, 2019, pp. 2265–2271.

[50] N. Aliyu, N. Ahmed, N. Stannard, and G. J. Atkinson, "Ac winding loss reduction in high speed axial flux permanent magnet machines using a lamination steel sheet," in *Proc. 2019 IEEE Int. Electric Machines Drives Conference (IEMDC)*, 2019, pp. 1053–1060.

[51] X. Wang, D. Liu, D. Lahaye, H. Polinder, and J. A. Ferreira, "Finite element analysis and experimental validation of eddy current losses in permanent magnet machines with fractional-slot concentrated windings," in *Proc. 2016 19th Int. Conf. on Electrical Machines and Systems (ICEMS)*, 2016, pp. 1–6.

[52] P. B. Reddy, T. M. Jahns, and T. P. Bohn, "Modeling and analysis of proximity losses in high-speed surface permanent magnet machines with concentrated windings," in *Proc. 2010 IEEE Energy Conversion Congress and Exposition*, 2010, pp. 996–1003.

[53] L. J. Wu and Z. Q. Zhu, "Simplified analytical model and investigation of open-circuit ac winding loss of permanent-magnet machines," *IEEE Trans. on Industrial Electronics*, vol. 61, no. 9, pp. 4990–4999, 2014.

[54] R.-J. Wang and M. Kamper, "Calculation of eddy current loss in axial field permanent-magnet machine with coreless stator," *IEEE Trans. on Energy Conversion*, vol. 19, no. 3, pp. 532–538, 2004.

[55] N. Taran, D. M. Ionel, V. Rallabandi, G. Heins, and D. Patterson, "An overview of methods and a new three-dimensional fea and analytical hybrid technique for calculating ac winding losses in pm machines," *IEEE Trans. on Industry Applications*, vol. 57, no. 1, pp. 352–362, 2021.

[56] H. Sano, T. Aasanuma, H. Katagiri, M. Miwa, K. Semba, and T. Yamada, "Loss calculation of bar-wound high-power-density pmsms with massively parallel processing," in *Proc. 2017 IEEE Int. Electric Machines and Drives Conference (IEMDC)*, 2017, pp. 1–6.

[57] B. Zhang, T. Seidler, R. Dierken, and M. Doppelbauer, "Development of a yokeless and segmented armature axial flux machine," *IEEE Trans. on Industrial Electronics*, vol. 63, no. 4, pp. 2062–2071, 2016.

[58] Magnax, *Axial flux vs radial flux: 4 reasons why axial flux machines have a higher power density*, Jun. 2, 2021. [Online]. Available: `https://www.magnax.com/magnax-blog/axial-flux-vs-radial-flux.-4-reasons-why-does-axial-flux-machines-deliver-a-higher-power-density`.

[59] L. Xu, Y. Xu, and J. Gong, "Analysis and optimization of cogging torque in yokeless and segmented armature axial-flux permanent-magnet machine with soft magnetic composite core," *IEEE Trans. on Magnetics*, vol. 54, no. 11, pp. 1–5, 2018.

[60] G. De Donato, F. Giulii Capponi, and F. Caricchi, "On the use of magnetic wedges in axial flux permanent magnet machines," *IEEE Trans. on Industrial Electronics*, vol. 60, no. 11, pp. 4831–4840, 2013.

[61] A. Krings, A. Boglietti, A. Cavagnino, and S. Sprague, "Soft magnetic material status and trends in electric machines," *IEEE Trans. on Industrial Electronics*, vol. 64, no. 3, pp. 2405–2414, 2017.

[62] R. Pei, L. Zeng, S. Li, and T. Coombs, "Studies on grain-oriented silicon steel used in traction motors," in *Proc. 2017 20th Int. Conf. on Electrical Machines and Systems (ICEMS)*, 2017, pp. 1–5.

[63] D. Kowal, P. Sergeant, L. Dupre, and A. Van den Bossche, "Comparison of nonoriented and grain-oriented material in an axial flux permanent-magnet machine," *IEEE Trans. on Magnetics*, vol. 46, no. 2, pp. 279–285, 2010.

[64] J. Ma, J. Li, H. Fang, *et al.*, "Optimal design of an axial-flux switched reluctance motor with grain-oriented electrical steel," *IEEE Trans. on Industry Applications*, vol. 53, no. 6, pp. 5327–5337, 2017.

[65] S. Kasai, M. Namikawa, and T. Hiratani, "Recent progress of high silicon electrical steel in jfe steel," JFE Steel, Tech. Rep., 2016, pp. 12–19.

[66] J.-Y. Soh, K.-Y. Shin, H. Jung, and S.-B. Kim, "Iron loss influenced by magnetic annealing in 0.1-mm-thick grain-oriented high-silicon steels," *IEEE Trans. on Magnetics*, vol. 47, no. 10, pp. 3208–3211, 2011.

[67] S. Takajo, T. Hiratani, T. Okubo, and Y. Oda, "Effect of silicon content on iron loss and magnetic domain structure of grain-oriented electrical steel sheet," *IEEE Trans. on Magnetics*, vol. 54, no. 1, pp. 1–6, 2018.

[68] A. Krings, M. Cossale, J. Soulard, A. Boglietti, and A. Cavagnino, "Manufacturing influence on the magnetic properties and iron losses in cobalt-iron stator cores for electrical machines," in *Proc. 2014 IEEE Energy Conversion Congress and Exposition (ECCE)*, 2014, pp. 5595–5601.

[69] Z. Wang, R. Masaki, S. Morinaga, *et al.*, "Development of an axial gap motor with amorphous metal cores," *IEEE Trans. on Industry Applications*, vol. 47, no. 3, 2011.

[70] M. A. Prabhu, J. Y. Loh, S. C. Joshi, *et al.*, "Magnetic loading of soft magnetic material selection implications for embedded machines in more electric engines," *IEEE Trans. on Magnetics*, vol. 52, no. 5, pp. 1–6, 2016.

[71] F. Kelch, Y. Yang, B. Bilgin, and A. Emadi, "Investigation and design of an axial flux permanent magnet machine for a commercial midsize aircraft electric taxiing system," *IET Electrical Systems in Transportation*, vol. 8, 52–60(8), 1 Mar. 2018.

[72] C.-W. Kim, G.-H. Jang, J.-M. Kim, J.-H. Ahn, C.-H. Baek, and J.-Y. Choi, "Comparison of axial flux permanent magnet synchronous machines with electrical steel core and soft magnetic composite core," *IEEE Trans. on Magnetics*, vol. 53, no. 11, pp. 1–4, 2017.

[73] D. Lin, P. Zhou, W. Fu, Z. Badics, and Z. Cendes, "A dynamic core loss model for soft ferromagnetic and power ferrite materials in transient finite element analysis," *IEEE Trans. on Magnetics*, vol. 40, no. 2, pp. 1318–1321, 2004.

[74] A. Corp, *Ansys maxwell*, Sofware, 2020. [Online]. Available: `https://www.ansys.com/products/electronics/ansys-maxwell`.

[75] D. Lin, P. Zhou, Z. Badics, W. Fu, Q. Chen, and Z. Cendes, "A new nonlinear anisotropic model for soft magnetic materials," *IEEE Trans. on Magnetics*, vol. 42, no. 4, pp. 963–966, 2006.

[76] G. Shirkoohi and J. Liu, "A finite element method for modelling of anisotropic grain-oriented steels," *IEEE Trans. on Magnetics*, vol. 30, no. 2, pp. 1078–1080, 1994.

[77] S. Magdaleno-Adame, T. D. Kefalas, A. Fakhravar, and J. C. Olivares-Galvan, "Comparative study of grain oriented and non–oriented electrical steels in magnetic shunts of power transformers," in *Proc. 2018 IEEE Int. Autumn Meeting on Power, Electronics and Computing (ROPEC)*, 2018, pp. 1–7.

[78] Z. Gmyrek, A. Cavagnino, and L. Ferraris, "Estimation of the magnetic properties of the damaged area resulting from the punching process: Exper-

imental research and fem modeling," *IEEE Trans. on Industry Applications*, vol. 49, no. 5, pp. 2069–2077, 2013.

[79] A. Boglietti, A. Cavagnino, L. Ferraris, and M. Lazzari, "The annealing influence onto the magnetic and energetic properties in soft magnetic material after punching process," in *Proc. IEEE Int. Electric Machines and Drives Conference, 2003. IEMDC'03.*, vol. 1, 2003, 503–508 vol.1.

[80] R. Sundaria, D. G. Nair, A. Lehikoinen, A. Arkkio, and A. Belahcen, "Effect of laser cutting on core losses in electrical machines—measurements and modeling," *IEEE Trans. on Industrial Electronics*, vol. 67, no. 9, pp. 7354–7363, 2020.

[81] W. Geng, Z. Zhang, and Q. Li, "High torque density fractional-slot concentrated-winding axial-flux permanent-magnet machine with modular smc stator," *IEEE Trans. on Industry Applications*, vol. 56, no. 4, pp. 3691–3699, 2020.

[82] Y. Zhao, D. Li, T. Pei, and R. Qu, "Overview of the rectangular wire windings ac electrical machine," *CES Trans. on Electrical Machines and Systems*, vol. 3, no. 2, pp. 160–169, 2019.

[83] D. A. Gonzalez and D. M. Saban, "Study of the copper losses in a high-speed permanent-magnet machine with form-wound windings," *IEEE Trans. on Industrial Electronics*, vol. 61, no. 6, pp. 3038–3045, 2014.

[84] P. Ponomarev, I. Petrov, N. Bianchi, and J. Pyrhönen, "Additional losses in stator slot windings of permanent magnet synchronous machines," Electronic Open-Access Publication, Tech. Rep., May 2015. DOI: 10.13140/RG.2.1.2081.9368.

[85] P. B. Reddy, T. M. Jahns, and A. M. El-Refaie, "Impact of winding layer number and slot/pole combination on ac armature losses of synchronous surface pm machines designed for wide constant-power speed range opera-

tion," in *Proc. 2008 IEEE Industry Applications Society Annual Meeting*, 2008, pp. 1–8.

[86] A. Riedel, M. Masuch, M. Weigelt, *et al.*, "Challenges of the hairpin technology for production techniques," in *Proc. 2018 21st Int. Conf. on Electrical Machines and Systems (ICEMS)*, 2018, pp. 2471–2476.

[87] A. Arzillo, P. Braglia, S. Nuzzo, *et al.*, "Challenges and future opportunities of hairpin technologies," in *Proc. 2020 IEEE 29th Int. Symposium on Industrial Electronics (ISIE)*, 2020, pp. 277–282.

[88] SKF, *Deep groove ball bearings*, Nov. 26, 2020. [Online]. Available: `https://www.skf.com/ca/en/products/rolling-bearings/ball-bearings/deep-groove-ball-bearings`.

[89] F. Wirth, C. Nguyen, J. Hofmann, and J. Fleischer, "Characterization of rectangular copper wire forming properties and derivation of control concepts for the kinematic bending of hairpin coils," *Procedia Manufacturing*, vol. 47, pp. 678–685, 2020.

[90] F. Wirth, T. Kirgör, J. Hofmann, and J. Fleischer, "Fe-based simulation of hairpin shaping processes for traction drives," in *Proc. 2018 8th Int. Electric Drives Production Conference (EDPC)*, 2018, pp. 1–5.

[91] A. Demiri, "Enamel insulated copper wire in electric motors: Sliding behavior and possible damage mechanisms during die bending," M.S. Thesis, Dept. of Mechanical. Automotive and Materials Engineering, University of Windsor, Windsor, Canada, 2014.

[92] T. Glaessel, J. Seefried, and J. Franke, "Challenges in the manufacturing of hairpin windings and application opportunities of infrared lasers for the contacting process," in *Proc. 2017 7th Int. Electric Drives Production Conference (EDPC)*, 2017, pp. 1–7.

[93] S. Engler, R. Ramsayer, and R. Poprawe, "Process studies on laser welding of copper with brilliant green and infrared lasers," *Physics Procedia*, vol. 12, pp. 339–346, 2011.

[94] M. Haubold, A. Ganser, T. Eder, and M. F. Zäh, "Laser welding of copper using a high power disc laser at green wavelength," *Procedia CIRP*, vol. 74, pp. 446–449, 2018.

[95] J. M. Rodríguez-Serna and R. Albarracín-Sánchez, "Numerical simulation of temperature and pressure changes due to partial discharges in spherical cavities within solid dielectrics at different ageing conditions," *Energies*, vol. 12, no. 24, 2019.

[96] Y. Wang, X. Yi, Y. Wang, *et al.*, "Partial discharge investigation of form-wound electric machine winding for electric aircraft propulsion," *IEEE Trans. on Transportation Electrification*, vol. 7, no. 1, pp. 78–90, 2021.

[97] N. Hayakawa and H. Okubo, "Partial discharge characteristics of inverter-fed motor coil samples under ac and surge voltage conditions," *IEEE Electrical Insulation Magazine*, vol. 21, no. 1, pp. 5–10, 2005.

[98] L. Benmamas, P. Teste, G. Krebs, E. Odic, F. Vangraefschepe, and T. Hamiti, "Contribution to partial discharge analysis in inverter-fed motor windings for automotive application," in *Proc. 2017 IEEE Electrical Insulation Conference (EIC)*, 2017, pp. 348–351.

[99] P. Pramod, A. Saha, K. Namburi, and R. Mitra, "Modeling, analysis and compensation of resistance imbalance in permanent magnet synchronous motor drives for mass manufacturing applications," in *Proc. 2019 IEEE International Electric Machines Drives Conference (IEMDC)*, 2019, pp. 1106–1109.

[100] J. Corp, *Jmag*, Sofware, 2020. [Online]. Available: `https://www.jmag-international.com/`.